High performance of electrosprayed graphene oxide/TiO_2/Ce-TiO_2 photoanodes for photoelectrocatalytic inactivation of *S. aureus*

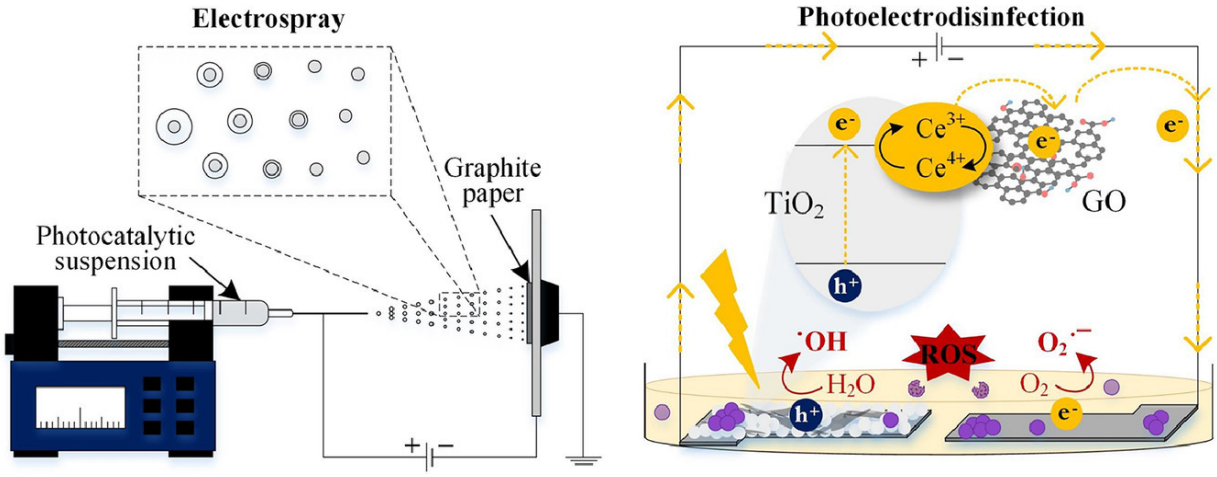

High performance of electrosprayed graphene oxide/TiO_2/Ce-TiO_2 photoanodes for photoelectrocatalytic inactivation of *S. aureus*

Laura Valenzuela[1,*], Marisol Faraldos[2], Ana Bahamonde[2], and Roberto Rosal[1]

[1]Department of Chemical Engineering, University of Alcalá, Alcalá de Henares, Madrid E-28871, Spain
[2]Instituto de Catálisis y Petroleoquímica, ICP-CSIC, Marie Curie 2, Madrid E-28049, Spain

Abstract

Microbial contamination is a challenging concern due to the health threat caused by infections. Therefore, the development of efficient antimicrobial materials and processes is a crucial need for disinfecting water and surfaces. In this study, electrospray was used to prepare composite photoanodes for photoelectrodisinfection. Titanium dioxide (TiO_2) and cerium-doped titanium dioxide (Ce-TiO_2) composites with Graphene Oxide (GO) were electrosprayed onto graphite paper to create homogeneous coatings of uniformly distributed nanoparticle aggregates with a layer thickness of 1.0–1.5 µm. The photoanodes were irradiated using 365 nm LED light with irradiance representing a conservative estimation of the UVA component of solar light. The external potential for electrocatalysis (dark) and photoelectrocatalysis was set at +0.6 V. The disinfection performance was assessed using anodes pre-exposed for 20 h in the darkness to exponentially growing cultures of *Staphylococcus aureus*. The highest antimicrobial activity was obtained for Ce-TiO_2/GO anodes, which led to a 3-log reduction (99.9 %) in the number of culturable cells after only 24 min of irradiation. The highest current density was also obtained for the same material and attributed to a better separation of charge carriers. Cell impairment was attributed to the overproduction of intracellular reactive oxygen species (ROS), which was higher in photoelectrocatalysis than in photocatalysis and electrocatalysis, with anodes performing in the following order: Ce-TiO_2/GO > Ce-TiO_2 > TiO_2/GO > TiO_2. The photoanodes exhibited steady photocurrent response, good photostability, and could be kept essentially clean from biofilms and colonizing bacteria.

1. Introduction

The emergence of new infectious diseases including the outspreading of antimicrobial resistances has become a global concern [1,2]. Microbial adhesion to surfaces is one of the main reasons for pathogen-associated infections as biofilm-forming bacteria can survive and proliferate in the most adverse environments [3]. The reason is that biofilms are the evolutive defence of bacteria against unfavorable environmental conditions. Biofilms are formed by highly structured communities with distinct morphologies and integrated metabolic activities controlled by a cascade of regulatory molecules; in fact, they are considered only one step below multicellular organisms [4]. Once attached to a surface, biofilms are very difficult to eradicate with the usual disinfection treatments, causing a high cost in terms of chemicals and other costs to keep safe clinical and food processing environments as well as to disinfect water and wastewater. Accordingly, there is a need to develop efficient antimicrobial materials and processes for disinfecting water and surfaces at a reasonable cost and with limited use of dangerous chemicals [5].

Antimicrobial materials should deactivate microorganisms in such a way that microbial attachment becomes inhibited. Besides, they should be capable to overcome the shortfalls of other disinfection methods like the appearance of resistances, the low lifespan of their action and the problems associated to microbial regrowth [6,7]. In some cases, the surface of interest can be chemically grafted with antimicrobial moieties. The covalent linkage of quaternary ammonium compounds and the in situ quaternization of tertiary amines are well-known approaches to create biofouling resistant surfaces [8]. With the same rationale, chitosan immobilized onto methacrylic acid-grafted polyurethane has been tested to create antimicrobial surfaces [5]. The antibacterial action of positively charged polymers can be attributed to the interaction with the negatively charged microbial envelopes [9]. Non-charged moieties have also been explored like sophorolipids derivatives used for glycosylating surfaces with antimicrobial coatings [10]. However, surface functionalization is a passive method that cannot be generally applied to disinfect air or aqueous streams and that becomes ineffective if the surface is

* Corresponding author: laura.valenzuela@uah.es
Available online: September 3, 2021

covered by dirt of by a first layer of early colonizers.

The use of engineered nanoparticles to create functional coatings has been the subject topic of intense research. Metal and metal oxide nanoparticles (NPs) such as Cu, Ag, TiO_2, ZnO, and many combined systems have been tested for antimicrobial applications [11]. The use of NPs is favored by their large surface-to-volume ratio and increased reactivity compared to their bulky counterparts, which result in the generation of Reactive Oxygen Species (ROS) including superoxide, hydrogen peroxide and hydroxyl radicals. ROS are known to impair microorganisms by damaging essential cellular components like membrane lipids, proteins and genetic materials [12]. The coating of target surfaces with antimicrobial photocatalytic NPs has been tested with semiconductor oxides like TiO_2 and ZnO. Surface functionalization using lithography techniques allowed creating antibacterial micropatterned surfaces onto medical-grade stainless steel using TiO_2 NPs, which significantly reduced the adhesion of Streptococcus mutans when activated by 350 nm (UVA) black light [13]. Zinc oxide–reduced graphene oxide (ZnO-rGO) nanocomposites were used to create photobiocidal surfaces by spin-coating. Such ZnO-rGO coatings proved high activity against *Staphylococcus aureus* with 5-log reduction of colony forming cells upon UVA irradiation with a conservative estimation of the UV component of the solar spectrum, which was attributed to the combination of photogenerated ROS and Zn^{2+} ions leaching [14].

Photoelectrocatalysis attempts to reduce charge carrier recombination by applying a bias potential that facilitates the drain of excited electrons in the correct direction, increasing their mobility and lifetime. The enhancement of photocatalytic activity also results in a higher antimicrobial efficiency. Photoanodes of TiO_2 including ordered TiO_2 nanotubes have proved capacity to successfully reduce the number of colony-forming units of different bacteria by several orders of magnitude [15-17]. Some research efforts tried to improve the photocatalytic efficiency by selective doping or decorating photoanodes with different metals [18-20]. The creation of heterojunctions is another way of facilitating the separation of photo-generated charges and the broadening of the irradiation spectrum to visible wavelengths [21, 22]. A disadvantage of most of the proposed arrangements is the limited stability of electrodes [23]. In this work we created a uniform packing of photocatalytic particles using electrospray, a electrohydrodynamic technique in which a suspension is ejected through a capillary while keeping a constant external electric field usually in the tens of kV range and generally operating in direct current mode [24]. The electric field creates small droplets that, ejected from the positively charged capillary, impact at high speed against a grounded collector [25]. Using this technique, a uniform distribution of small particles can be precisely created onto a conductive substrate with morphology that depends on the electrohydrodynamic parameters and system properties [26-28]. Electrosprayed coatings demonstrated effectiveness to create antibacterial photoactive surfaces [29, 30].

TiO_2 nanoparticulate electrodes (generally prepared by physical deposition methods such as spin-coating, dip-coating or spray-coating) have been reported not to exhibit an efficient charge carrier separation and thus not to enhance photocatalytic performance when applying an anodic bias potential as compared with nanostructured electrodes like vertically aligned TiO_2 nanotube array films fabricated by electrochemical anodization [31-33]. This hindered charge carrier separation has been attributed to the partial sintering of the particles that hampers the diffusion of photoexcited electrons from the photocatalyst surface to the conductive substrate preventing the development of a potential gradient [34]. During electrospray, the deposited particles keep an electric charge that influences the assembly of subsequent particles, thereby creating a nanostructure with specific morphology and high roughness [35]. Therefore, as in electrochemical anodization, structures with electron transport capability and good connection throughout the substrate allowing charge carrier separation are expected to be formed by electrospray [36]. Moreover, electrospray has advantages over anodization since it offers the possibility of using any electrically conducting substrate and easily obtaining nanocomposite films with intimate interfacial contact between their constitutive active phases.

In this work, we demonstrated the capacity of electrosprayed TiO_2/Ce-TiO_2/graphene oxide anodes in a photoelectrocatalytic arrangement to inhibit bacterial growth even under the very unfavorable conditions created by previous exposure to exponentially growing cultures of *S. aureus*. The irradiation used was a conservative estimation of the UVA component of solar light. Cell damage was evaluated by viable colony counting, by measuring the metabolic activity of cells, and by tracking the overproduction of ROS.

2. Experimental

2.1 Chemicals and materials

Titanium tetraisopropoxide (TTIP, $\geq$ 97 %) and cerium (III) nitrate hexahydrate ($\geq$ 99 %) were purchased form Sigma-Aldrich. Graphene Oxide (GO) water dispersion (0.4 wt% concentration) was acquired from Graphenea (Spain). SIGRACELL® PV15

bipolar plates were obtained from SGL Carbon (Germany). Fluorescein diacetate (used as cell viability stain) and 2′,7′-dichlorodihydrofluorescein diacetate ($\geq$ 97 %) were also procured from Sigma-Aldrich. The reagents of biological media and buffers were purchased from Conda lab (Madrid). Ultrapure water (Millipore Milli-Q System, > 18 mΩ cm) was used in all experiments.

2.2 Synthesis and characterization of photocatalytic materials

TiO_2 nanoparticles were prepared by sol-gel method, typically 8.25 mL of titanium tetraisopropoxide were added dropwise to 100 mL acidified water (140:1 water to nitric acid) under vigoros stirring [37]. After ageing for three days, a stable sol was obtained with 20 wt% TiO_2. Cerium suspension was prepared according to a procedure previously described [38]. Briefly, 13 mM cerium (III) nitrate hexahydrate was dissolved in 20 mL of water, absolute ethanol, and nitric acid (5:5:1 in volume). In order to obtain the 1.5 wt% Ce and/or 2 wt% GO nanocomposites, corresponding amounts of cerium sol or/and GO water dispersion (0.4 wt% concentration) were added prior to the incorporation of the titanium precursor and the resultant suspensions allowed to age until complete peptization (3 days for TiO_2 and Ce-TiO_2 sols and 50 days for suspensions containing GO). Therefore, the nucleation and growth of TiO_2 could occur on the graphene sheets due to the interaction between Ti^{4+} and the oxygen-containing functional groups of GO, resulting in higher photocatalytic efficiency [39].

Dynamic particle size and surface charge (ζ-potential) were measured by Dynamic Light Scattering (DLS) at 25 °C using a Zetasizer Nano ZS Instrument. pH and electrical conductivity were measured using a MM 40+ multimeter (Crison). Surface tension was determined through the pendant drop technique by means of a Drop Shape Analyzer (DSA25, Krüss) using ImageJ software to process images. UV-vis Diffuse Reflectance Spectra (DRS) of the solid samples were recorded on an Agilent Cary 5000 equipment. X-ray Diffraction (XRD, PANalytical X'Pert Pro) analyses were performed to assess the crystal structure of the nanoparticle powders and crystallite size using the Scherrer's equation. Raman spectra were collected using a Renishaw InVia Raman microscope (532 nm, 10 s exposure, 10 % of laser power). TEM images were acquired in a JEOL 2100F. The elemental composition of the samples was confirmed by Energy Dispersive X-ray Spectroscopy (SEM-EDX, Hitachi TM-1000, and TEM-EDX, JEOL 2100F) and Inductively Coupled Plasma Atomic Emission Spectroscopy (ICP-AES, PlasmaQuant® PQ 9000, Analytik Jena) after 2 h acidic digestion in microwave oven.

2.3 Fabrication and characterization of electrosprayed anodes

The photocatalytic particles were electrosprayed onto sanded and prewashed 2.5 × 2.5 cm graphite paper (GP) substrates. The electrospraying parameters were adjusted in order to operate in a stable cone-jet mode, which is known to strongly depend on the physical properties of the suspensions and the liquid flow rate [40-42]. Briefly, the suspensions of photocatalytic particles were ejected through a stainless-steel blunt-tip capillary needle (0.337 mm inner diameter) at a constant flow rate of 0.05 mL h^{-1} by means of a Harvard PHD 22/2000 syringe pump. An aerosol of positively charged drops was generated from the positively charged needle tip and driven towards a grounded collector by supplying a high voltage of 22 kV (DC, Heinzinger LNC 30,000). The needle to collector distance was 20 cm and the relative humidity was kept in the 50–60 % range. A deposition time of 180 min was used to fabricate the photocatalytic films, which were characterized by Scanning Electron Microscopy (SEM, Zeiss DSM 950) at an accelerating voltage of 25 kV after gold coating. AFM images of electrosprayed specimens were obtained using atomic force microscopy (AFM) in an Agilent 5500 AFM/SPM apparatus operating in noncontact mode. AFM images were processed using WSxM 5.0 software. In order to evaluate the photoelectrochemical properties of the electrosprayed anodes, linear sweep voltammetry (LSV) and cyclic voltammetry (CV) were performed in a three-electrode cell configuration (working volume: 20 mL), employing graphite paper and Ag/AgCl as counter and reference electrodes, respectively. Both electrodes were placed horizontally 0.5 cm separated, while the tip of reference electrode was positioned close to the anode. A Metrohm Autolab PGSTAT101 was used for LSV and CV with a scan rate of 5 mV s^{-1}. Ten consecutive LSV and CV scans were conducted with the same electrode, five in the dark and five in the presence of light irradiation.

2.4 Disinfection experiments and bioanalytical procedures

Disinfection studies were carried out using the biofilm-forming gram-positive bacterium *Staphylococcus aureus* (CECT 240). *S. aureus* was grown in Nutrient Broth (NB, 5 g L^{-1} beef extract, 10 g L^{-1} peptone, 5 g L^{-1} NaCl, pH 7.0 ± 0.2) while shaking at 37 °C. Then, the electrochemical cell was inoculated to reach 106 cell mL^{-1} using 1/10 NB as electrolyte (electrical conductivity: 1209 ± 26 µS cm^{-1}) and incubated for 20 h at 37 °C in the dark. This procedure yielded colonization of electrodes with

extensive biofilm formation. Disinfection runs were conducted while operating in three-electrode configuration starting from electrodes colonized by bacteria.

Three different disinfection treatments were performed: (i) electrocatalytic (EC, bias potential only), (ii) photocatalytic (PC, UV-irradiation only), and (iii) photoelectrocatalytic (PEC, bias potential + irradiation). For comparison, control tests (without any treatment) were carried out under the same experimental conditions. Chronoamperometry (CA) curves were recorded during EC and PEC disinfection treatments. The external potential was set at +0.6 V vs. the reference electrode and the cell was irradiated using a 365 nm UV light source (LED BLS 13,000^{-1}, Mightex). The irradiance for PC and PEC assays was selected at 3.0 kW-h m^{-2} day^{-1}, chosen as a conservative estimation representing 1/2 of the 25th percentile of the solar irradiance in the 280–400 nm wavelength range (5.2 % of the total solar irradiance) as calculated for the latitude of Madrid (40.42 °N) using NASA's POWER project data (https://power.larc.nasa.gov/). This daylight exposure condition was simulated by adjusting exposure time and spot diameter of the UV lamp. For 100 mm diameter spot (i.e. the minimum spot required for a correct illumination of the experimental system used), the estimated exposure time was 24 min (24 min = 1 day). For this reason, 24 min were selected as the duration for all the disinfection treatments carried out in the exposed study.

The number of viable bacteria both in the liquid and attached to the surface of the electrodes was determined by plate counting according to the standard ISO 22,196. To remove non-adhered bacteria and recover those attached to the surfaces, the electrodes were transferred to 6-well plates first containing PBS (phosphate buffered saline) for 15 min and treated subsequently with SCDLP broth (Soybean casein digest broth with lecithin and polyoxyethylene sorbitan monooleate) for 30 min. 10 µL spots of 10-fold serial dilutions were placed on agar plates (2.5 g L^{-1} yeast extract, 5 g L^{-1} tryptone, 1 g L^{-1} glucose, 15 g L^{-1} agar powder) and incubated at 37 °C for 24 h. The number of colony-forming units (CFU) was calculated using at least three replicates of at least two serial dilutions.

Bacterial viability was also assessed using fluorescein diacetate (FDA), a non-fluorescent compound which is hydrolyzed by intracellular esterases in functional cells yielding the green fluorescent fluorescein. Upon disinfection treatment, 5 µL of FDA (0.02 wt% in dimethyl sulfoxide) were added to 195 µL of bacterial suspension in black 96-well microplates and incubated at 25 °C for 25 min. Additionally, intracellular oxidative stress was tested using dichlorofluorescein (DCF) as an indicator. Briefly, 150 µL of culture medium after disinfection treatment were transferred to black 96-well plates with 50 µL of a 10 mM 2',7'-dichlorodihydrofluorescein diacetate (H_2DCFDA) solution and subsequently incubated at 25 °C for 30 min. H_2DCFDA penetrates into the cytoplasm and is hydrolyzed to dichlorodihydrofluorescein carboxylate anion, which is further oxidized to the fluorescent DCF in the presence of ROS [43,44]. To perform both fluorescence-based assays, a fluorometer (Fluoroskan Ascent FL, Thermo Scientific) was used with excitation/emission wavelengths of 485 and 528 nm, respectively.

2.5 Statistical analysis

Statgraphics centurion XVII software was used to perform a one- or two-way analysis of variance (ANOVA). Mean comparison was performed using Tukey's test ($p < 0.05$), while Grubbs' test was used to find the outliers following the ASTM E178-00 standard. Results are provided as average plus/minus standard deviation.

3.Results and discussion

3.1 Photocatalysts properties and electrospray parameters

During the electrospray deposition process, charged droplets lose solvent during their path from the capillary exit to grounded collector. Consequently, charge density increases, until reaching the Rayleigh limit for which electrostatic repulsion overcomes surface tension and causes the fission of droplets into a multiplicity of smaller ones [25]. The breaking up into small droplets is favored if surface tension is low, which limits the applicability of electrospray to aqueous solutions or suspensions due to the relatively high surface tension of water [45-47]. Therefore, the electrospray suspensions were prepared in 50 % v/v ethanol-water mixture, which resulted in surface tension to about 30 mN m^{-1} (from values > 50 mN m^{-1} before dilution with ethanol), low enough to produce adequate electrospraying without the addition of surfactants (Table 1). As shown in Fig. S1 (Supplementary Material, SM), DLS particle size measurements displayed a well-defined single peak at 103.4 ± 2.2 nm for TiO_2 and 337.1 ± 12.9 nm for Ce-TiO_2 suspensions, respectively. The higher particle size of the Ce-TiO_2 photocatalyst could be attributed to cerium acting as nucleation site in the sol-gel synthesis as it was added prior to TTIP in the sol-gel synthesis method used (see Experimental section). It has been previously described that Ce can inhibit crystal growth of anatase TiO_2 to decrease crystal

size but favor colloids aggregation to increase particle size [48]. However, the suspensions of nanocomposites containing GO, TiO_2/GO and Ce-TiO_2/GO, exhibited bimodal size distribution, with dominant sizes of aggregates/agglomerates of 1339 ± 67 nm and 1798 ± 134 nm and secondary peaks at 101.8 ± 5.2 nm and 302.5 ± 52.7 nm, which could be attributed to decorated GO sheets and bare TiO_2 and Ce-TiO_2 nanoparticles, respectively (Fig. S1, SM). Fig. S2 (SM) shows, for reference, an image of Ce-TiO_2 particles bound to GO sheets. TiO_2 nanoparticles in the sol were positively charged at the acidic pH of the electrospraying suspensions, displaying a ζ-potential of +11.6 ± 1.8 mV, which barely changed after the incorporation of Ce and GO. Interestingly, the electrical conductivity increased from 5.08 ± 0.92 and 5.16 ± 0.01 mS cm^{-1} for TiO_2 and TiO_2/GO to 11.45 ± 0.41 and 17.34 ± 0.82 mS cm^{-1} for Ce-TiO_2 and Ce-TiO_2/GO, probably due to the presence of electroactive cerium species [49,50].

The optical properties of TiO_2 nanocomposites were evaluated by DRS, as shown in Fig. S3a (SM). The characteristic absorption edge of TiO_2 was observed at about 398 nm, corresponding to the promotion of electrons from valence to conduction band. After coupling to Ce or GO sheets, the absorption edge redshifted and visible light absorption enhanced as compared to pristine TiO_2. The corresponding indirect band-gaps were calculated through Kubelka-Munk function combined with Tauc's relation and baseline method (Fig. S3b, SM) [51,52]. The estimated band-gap energies were 3.08, 3.09, 3.17 and 3.18 for TiO_2, Ce-TiO_2, TiO_2/GO and Ce-TiO_2/GO, respectively. The presence of Ce and/or GO hardly modified the band-gap energies of the semiconductor as all the photocatalysts exhibited similar values to bare TiO_2.

The crystal structure of the photocatalytic materials was investigated by XRD (Fig. 1). All the composites displayed similar diffraction patterns, which can be ascribed to the anatase structure of TiO_2 (JCPDS 00-021-1272). Moreover, TiO_2 nanoparticles exhibited peaks at 30.8°, corresponding to (121) plane of TiO_2 brookite phase (JCPDS 00-016-0617), and 35.5°, attributed to (101) plane of rutile TiO_2 (JCPDS 01-076-0325). No diffraction peaks related to Ce and GO were detected in the composites probably because of their low loading and the strong diffraction intensity from anatase TiO_2 [53-55]. Nevertheless, the presence of both Ce and GO favored rutile TiO_2 formation with the appearance of two additional diffraction peaks located at 27.1° and 40.6°, which can be indexed to the (110) and (111) planes, respectively (JCPDS 01-076-0325). Regarding the Ce-TiO_2 photocatalyst, the promotion of rutile TiO_2 phase formation could be explained by Ce ions introducing substitutionally in the network, which is known to create oxygen vacancies thus promoting anatase to rutile transition due to some extra space available [56]. However, despite multi-technique characterization analysis, it could not be verified how the Ce-doping interacts within the TiO_2 network. Referring to GO, it has been reported to inhibit anatase to rutile phase transition due to its high surface area and the interaction between Ti^{4+} and the oxygen-containing functional groups of GO [57]. Nevertheless, the much longer peptization time required for suspensions containing GO could have resulted in some rutile phase formation [58]. Interestingly, the more noticeable anatase to rutile TiO_2 phase transition in Ce-TiO_2 was dampened by GO incorporation probably due to physical interactions occurring between Ce and GO components prior to TTIP addition [59], which could lead to an enhanced photocatalytic performance of Ce-TiO_2/GO composite compared to the two-component photocatalyst since anatase is more active in this process than rutile [60]. The calculated crystallite sizes using the Debye-Scherrer equation were 5.3, 5.7, 5.5 and 5.9 nm for anatase TiO_2 in the TiO_2, TiO_2/GO, Ce-TiO_2 and Ce-TiO_2/GO photocatalytic materials, respectively, barely changing after Ce and/or GO incorporation to TiO_2.

Raman spectroscopy was performed on TiO_2, TiO_2/GO, Ce-TiO_2 and Ce-TiO_2/GO photocatalysts to confirm phase composition (Fig. 2). Raman bands at 155, 410, 515 and 636 cm^{-1} corresponded to the E_{g1}, B_{1g}, A_{1g} and E_{g2} modes of anatase TiO_2 (space group of $I41/amd$) [61,62]. Mixed phases of anatase and rutile Raman modes were only observed for Ce-TiO_2 with the emergence of two additional bands at 445 and 610 cm^{-1}, which were assigned to the E_g and A_{1g} modes of rutile TiO_2 (space group of $P42/mnm$) [63]. TiO_2/GO and Ce-TiO_2/GO spectra exhibited the characteristic *D* (disordered carbon) and *G* bands (graphitic sp^2 carbon) of graphitized structures at 1344 and 1606 cm^{-1}, respectively, and smaller bands at 2714 (2*D* band) and 2962 cm^{-1} (*D*+*G* band) [64].

The elemental composition of the photocatalytic materials was determined by EDX (Figs. S4 and S5, SM) and ICP-AES. Ce-TiO_2 and Ce-TiO_2/GO EDX spectra displayed peaks corresponding to Ti and Ce, confirming the incorporation of Ce into the TiO_2 photocatalyst. Moreover, TEM images show crystalline domains of anatase with lattice spacing of 3.52 Å, calculated using Fast Fourier Transform (FFT) and consistent with the (101) lattice plane of anatase phase, and aggregates of crystallites typically with size < 10 nm (Fig. S5, SM). These results are consistent with the anatase crystallite size calculated from XRD peak width (FWMH) and confirms the small

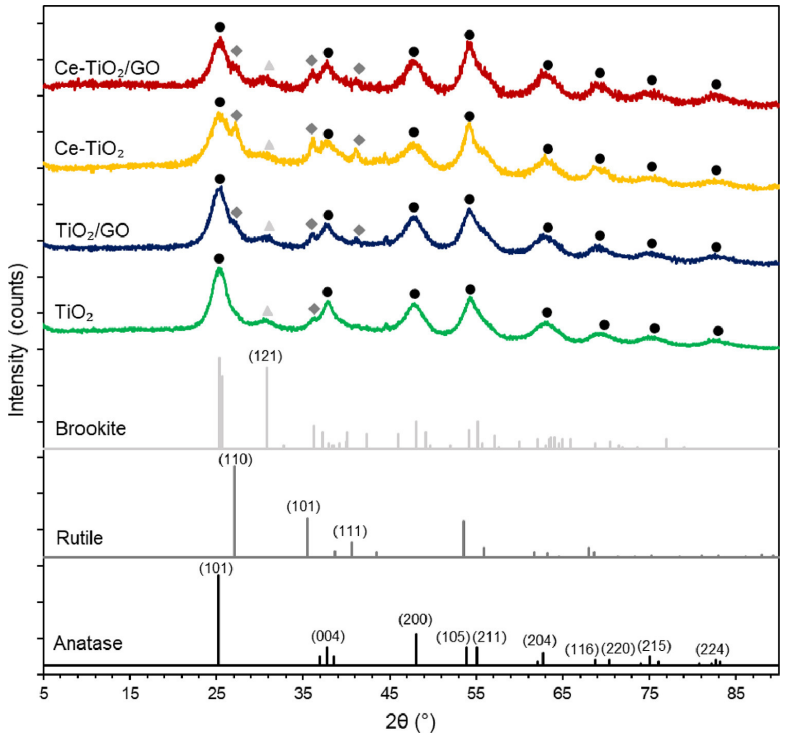

Figure 1: *X-ray diffraction patterns of TiO_2 , TiO_2/GO , Ce-TiO_2 and Ce-TiO_2/GO . Green, blue, yellow and red squares for TiO_2, TiO_2/GO, Ce-TiO_2 and Ce-TiO_2/GO, respectively.*

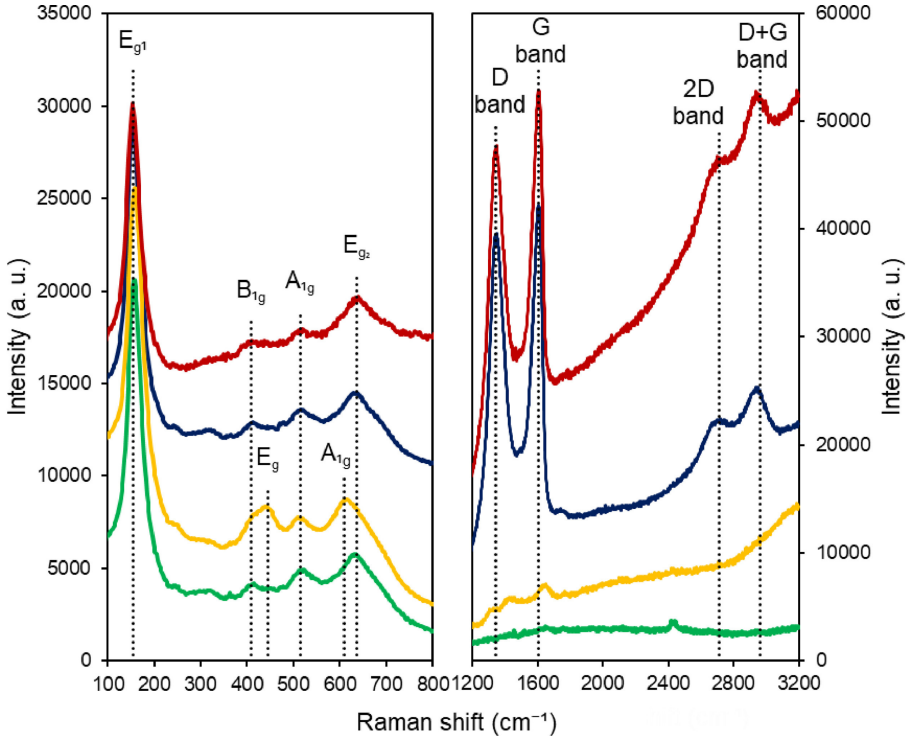

Figure 2: *Raman spectra of TiO_2 , TiO_2/GO , Ce-TiO_2 and Ce-TiO_2/GO . Green, blue, yellow and red squares for TiO_2, TiO_2/GO, Ce-TiO_2 and Ce-TiO_2/GO, respectively.*

Table 1. *Physicochemical properties of photocatalysts.*

	TiO_2	TiO_2/GO	Ce-TiO_2	Ce-TiO_2/GO
DLS Particle size (nm)	103.4 ± 2.2	1339 ± 67 (83 %)	337.1 ± 12.9	1798 ± 134 (93%)
		101.8 ± 5.2 (17 %)		302.5 ± 52.7 (7 %)
ζ-Potential (mV)	+11.6 ± 1.8	+10.4 ± 1.0	+8.9 ± 0.5	+9.4 ± 0.8
pH	1.85 ± 0.02	1.69 ± 0.04	1.30 ± 0.02	1.13 ± 0.03
Electrical conductivity (mS cm^{-1})	5.1 ± 0.9	5.16 ± 0.01	11.5 ± 0.4	17.3 ± 0.8
Surface tension (mN m^{-1})	33.1 ± 0.5	32.7 ± 0.6	33.4 ± 0.1	30.7 ± 0.2
Band-gap (eV)	3.08	3.17	3.09	3.18
XRD anatase crystallite size (nm)	5.3	5.7	5.5	5.9

size of peptized TiO_2 nanoparticles. In this regard, DLS size (Table 1 and Fig. S1) corresponds to aggregates of these crystalline nanoparticles originated by interaction among TiO_2 crystallites to minimize surface energy and form a stable suspension. The interplanar spacing of GO was calculated from the diffraction peak at 11.06 ° as 8.00 Å, corresponding to the (001) reflection plane of graphene oxide (Fig. S6, SM).

The electron diffraction (SAED) analysis only exhibited the majority anatase phase, which could be ascribed to the high dispersion and low concentration of Ce. The concentration of Ce in the Ce-TiO_2 and Ce-TiO_2/GO photocatalysts quantified by ICP-AES was 1.27 ± 0.01 and 0.92 ± 0.01 wt% (95 % confidence level), respectively. Due to the low Ce concentration used in this work, no XPS evidence could be obtained on the presence of Ce (III) and Ce (IV) oxidation sates, but a number of previous works obtained clear proofs about their simultaneous presence in Ce-TiO_2 photocatalysts [38, 65-67].

3.2 Characteristics of electrosprayed anodes

Surface morphology and cross-sectional views of electrosprayed anodes were obtained from SEM images as shown in Fig. 3. Top views displayed a uniformly distributed pattern of nanoparticle aggregates onto graphite paper (a SEM image of sanded graphite paper is presented in Fig. S7, SM) with a diameter in the submicron range. The morphology, grain size and agglomeration state of the nanoparticles were influenced by the incorporation of GO sheets, which resulted in TiO_2/GO and Ce-TiO_2/GO composites with considerably higher surface roughness. The thickness of the photocatalytic surfaces was estimated to be about 1.0–1.5 µm as determined from cross-sectional images with negligible differences between nanomaterials. AFM allowed some calculation related to the morphology of the electrode surface. An image corresponding to the Ce-TiO_2/GO electrode is shown in Fig. S8 (SM). Rounded particles of 300–500 nm diameter were compatible with the grain size shown in Fig. 3 and the DLS particle size measurements described in Section 3.1. Flat areas were most probably due to GO sheets also visible in Fig. S2 (SM). Roughness, calculated as RMS (Root Mean Square) roughness, was 45.7 nm with many irregularities displaying heights of 100 nm or higher as shown in the profile displayed in Fig. S8 B (SM). Overall, the surface was considerably rougher than similar coatings prepared by other techniques like sol-gel spin-coating [68, 69].

The photoelectrochemical response of TiO_2, TiO_2/GO, Ce-TiO_2, and Ce-TiO_2 electrosprayed anodes was investigated by recording LSV and CV curves in 1/10 NB at 5 mV s^{-1} under abiotic and biotic conditions and in the absence and presence of UV light irradiation. The results of LSV are shown in Fig. 4, while CV curves are displayed in Fig. S9 (SM). Compared with uncoated graphite paper electrodes, lower current densities were obtained for functionalized anodes due to the presence of a semiconductor layer providing electron transfer resistance. A similar behavior was observed in tests carried out under biotic conditions, suggesting that biofilm acted as a barrier not only to light harvesting but also to electron transfer [70, 71]. LSV and CV curves displayed increased current density under UV irradiation for all electrosprayed electrodes, demonstrating their photoelectrochemical activity. For all the photoanode materials tested, the onset of the process was observed at the same potential (+0.7 V vs. Ag/AgCl) irrespective of the presence or absence of bacteria, UV light irradiation and photocatalytic coating, suggesting that it should be attributed to the beginning of oxygen evolution reaction (OER). As the indirect oxidation by ROS is based on oxygen evolution intermediates, OER is an unwanted side reaction that may take also place at the anode causing a decrease in overall current efficiency. Carbon-based electrodes (e.g. graphite paper) are characterized by a low oxygen evolution overpotential, which favors the transformation of physically adsorbed hydroxyl radicals into the much weaker oxidant chemisorbed 'active

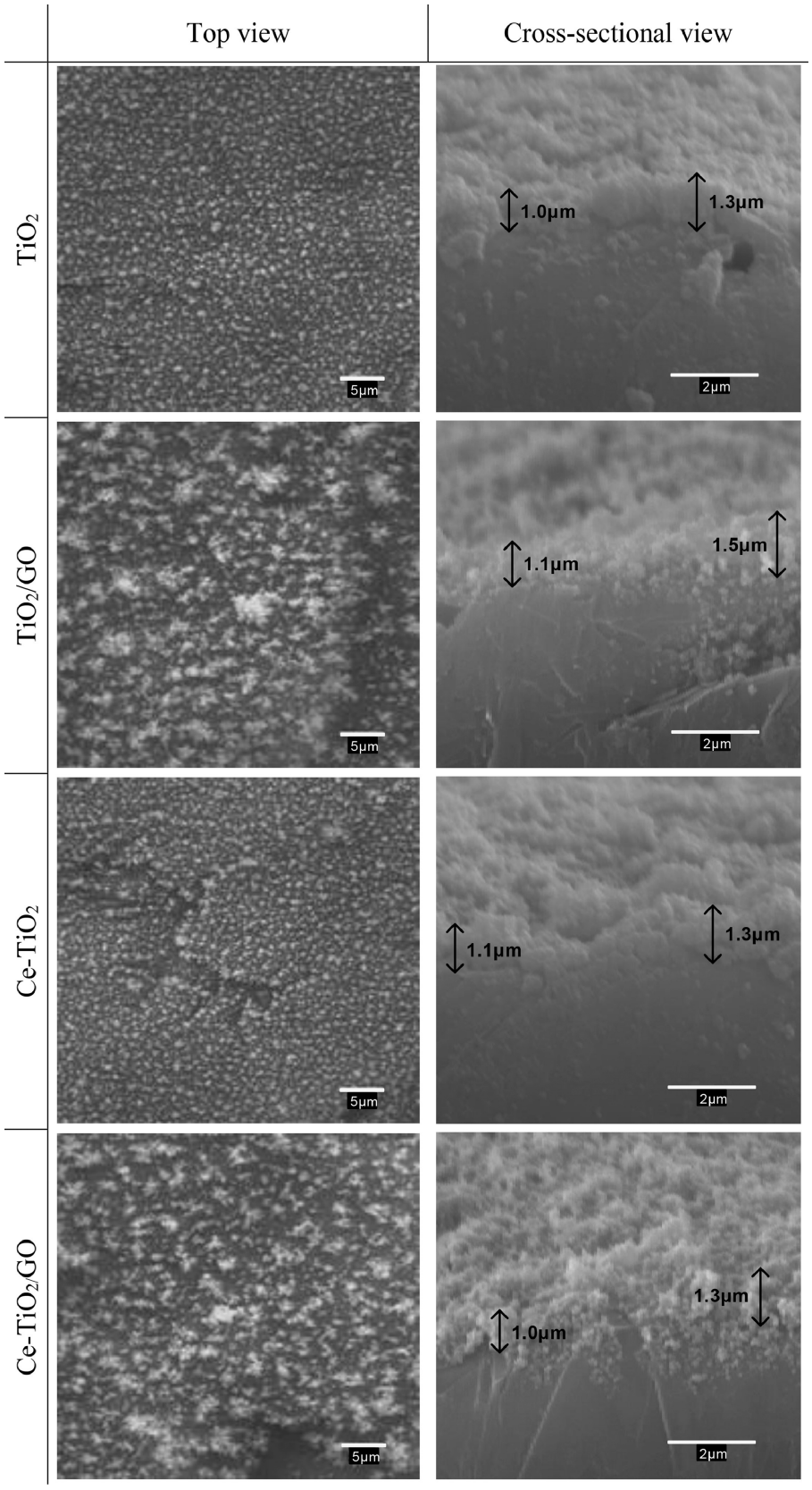

Figure 3: *Top and cross-sectional SEM images of TiO_2, TiO_2/GO, Ce-TiO_2 and Ce-TiO_2 electrosprayed anodes.*

oxygen' or superoxide. Therefore, in these cases, effective oxidation occurs at low current densities [72]. Moreover, in the case of TiO_2 and TiO_2/GO photocatalytic anodes, photocurrent increased up to +0.6 V vs. Ag/AgCl, to decrease thereafter. Accordingly, +0.6 V was selected as operating potential for disinfection experiments. Upon addition of 2 wt% GO, photocurrent slightly increased compared with pristine TiO_2 (especially at E > +0.6 V vs. Ag/AgCl), which could be attributed to improved electron mobility [73, 74]. In order to obtain a better observation of these differences, Fig. S10 (SM) presents current density values at +0.6 V vs. Ag/AgCl obtained from LSV curves. Interestingly, Ce-TiO_2 and Ce-TiO_2/GO nanocomposite electrodes displayed higher capacitive current (dark) around +0.6 V vs. Ag/AgCl and photocurrent density steadily increased with increasing anodic potential from 0 to +0.8 V. It has been previously shown that the incorporation of Ce enhances visible light absorption and supresses charge recombination of TiO_2 [49, 50, 75]. However, in this work, the obtained photocurrent was lower for Ce-TiO_2 functionalized anodes, which could be attributed to a lower photoresponse in the near-UV region. In PEC, also known as electrochemically assisted photocatalysis, the applied potential promotes photoexcited electrons from the conduction band of the semiconductor to the counter electrode or cathode through the external circuit while holes accumulate on the photoanode surface. Consequently, an anodic photocurrent is generated, and oxidation and reduction reactions are spatially separated leading to higher quantum yields and faradaic efficiencies. The highest current density value under UV illumination at E $\geq$ +0.6 V vs. Ag/AgCl was obtained for the three-component Ce-TiO_2/GO photocatalytic anodes, meaning an improved charge carrier separation [49, 50]. Furthermore, electrospray has been demonstrated to produce stable binder-free catalytic electrodes [36]. Fig. S11 (SM) displays the overlay CV curves for the ten cycles performed with Ce-TiO_2/GO anode under abiotic conditions. As can be observed, after the two previous conditioning cycles, no noticeable differences were found between successive cycles both in darkness and in the presence of UV light, proving the good photoelectrochemical stability of the as-prepared anodes under the used experimental conditions.

3.3 Disinfection performance

The photoelectrochemical disinfection performance of TiO_2, TiO_2/GO, Ce-TiO_2 and Ce-TiO_2 anodes was evaluated against *S. aureus* by quantifying CFU reduction in the liquid medium and on the electrodes surface (Figs. 5 and S12, SM). Negligible bactericidal activity was obtained for all the photocatalysts tested without performing any treatment (controls), proving their high stability in aqueous media and thus excellent film durability. TiO_2-based photocatalysts are known not to exhibit leaching problems resulting more appropriate for the safe water disinfection than other photocatalysts such as ZnO [76, 77]. For PC and PEC treatments with TiO_2 and TiO_2/GO photocatalytic anodes, > 88 % inhibition (1-log reduction) was achieved in the liquid electrolyte (Fig. 5a) compared to controls. Higher CFU reduction (2-log) was obtained for anodes including Ce. Despite its lower photocurrent obtained under 365 nm wavelength irradiation, Ce-TiO_2 electrosprayed anodes exhibited higher disinfection performance than pristine TiO_2 and TiO_2/GO composite. The effect, also observed for EC runs, could be attributed to the cycling between Ce^{4+} and Ce^{3+} oxidation states, which favors the mobility of electrons [38, 78]. The best results (3-log or 99.8 % reduction) were obtained for Ce-TiO_2/GO anodes. The better EC performance obtained for Ce-TiO_2 as compared to Ce-TiO_2/GO might be related to the larger rutile/anatase ratio in the Ce-TiO_2 catalyst, as observed in XRD and Raman spectroscopy results (Figs. 1 and 2). Although anatase is more active in photocatalytic processes than rutile, it has been previously reported that mixed phases of anatase and rutile TiO_2 exhibited higher electrochemical activity than pure anatase [79]. Appropriate proportions of anatase and rutile have shown to improve the dispersion rate of electrons due to the crystal interface effect and decrease charge transfer limitations owing to the conversion of Ti^{4+} into Ti^{3+} through the formation of the rutile phase [79, 80]. For cells attached to surface of the anodes (Fig. 5b), PEC process led to > 95 % CFU reduction, outperforming significantly PC and EC disinfection treatments for the same reactor configuration ($p < 0.05$), which suggested that charge carrier recombination could be effectively suppressed by applying an anodic bias potential to the irradiated photocatalysts [81, 82]. In the case of bacteria adhered to the GP cathodes (Fig. S12, SM), the differences between treatments and photocatalytic materials were limited and, in fact, not significant for p-values $\leq$ 0.05.

The higher performance of PEC disinfection process as compared to PC treatment using TiO_2 anodes has been previously reported. Salmerón et al. employed TiO_2 nanotubes on Ti mesh and carbon felt as photoanode and cathode, respectively, for the simultaneous degradation of microcontaminants and *E. coli* inactivation, achieving 2.7 and 0.8-log reduction in 90 min for PEC and PC treatments [83]. Although mean log removal was negligible for

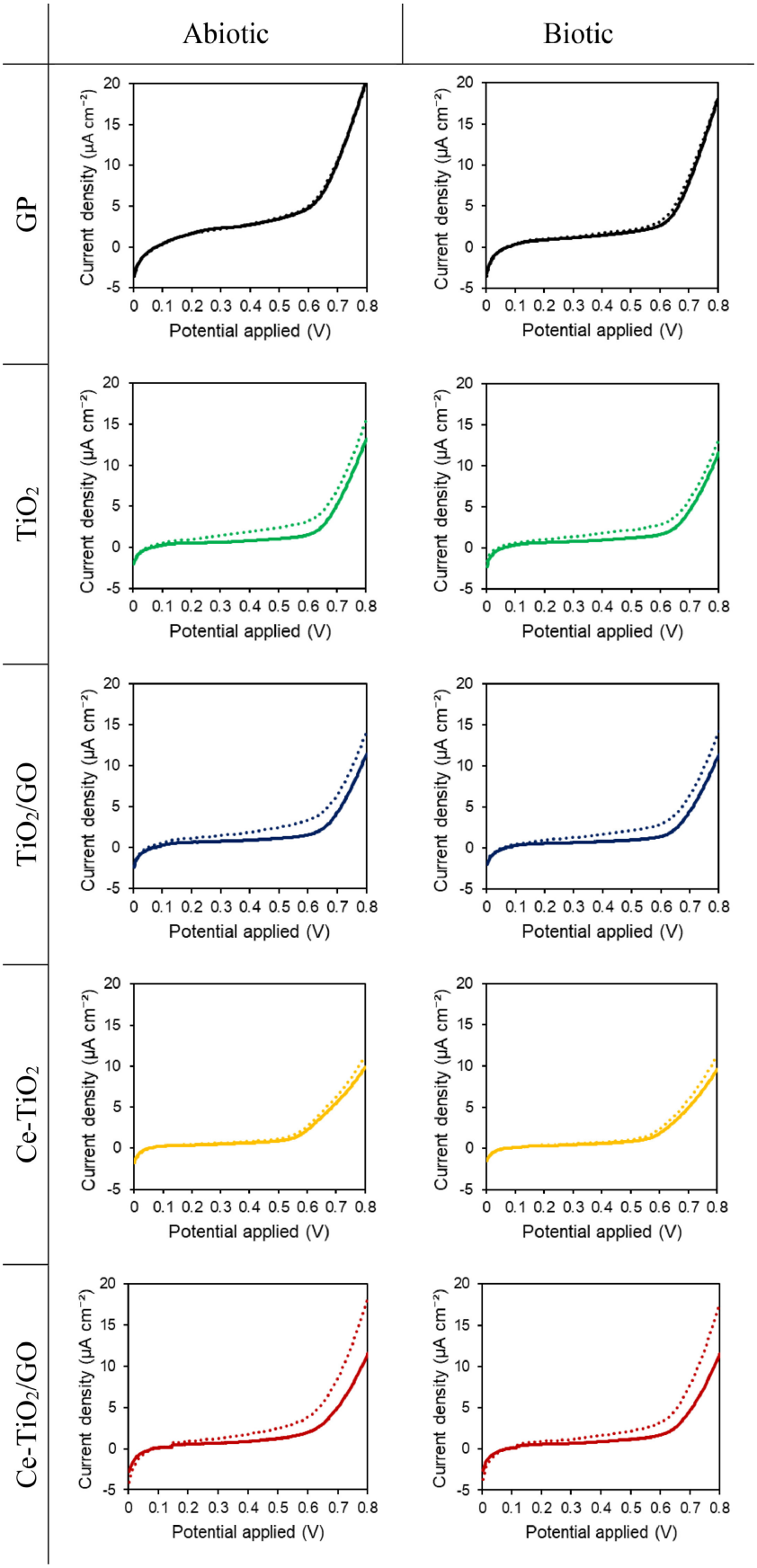

Figure 4: *Linear sweep voltammetry (LSV) curves of GP, TiO_2, TiO_2/GO, Ce-TiO_2 and Ce-TiO_2 anodes in 1/10 NB at 5 mV s^{-1}, under abiotic and biotic conditions, in the absence (—) and presence (···) of UV light irradiation. The fifth LSV scan is displayed. Green, blue, yellow and red squares for TiO_2, TiO_2/GO, Ce-TiO_2 and Ce-TiO_2, respectively.*

(a) [liquid medium]

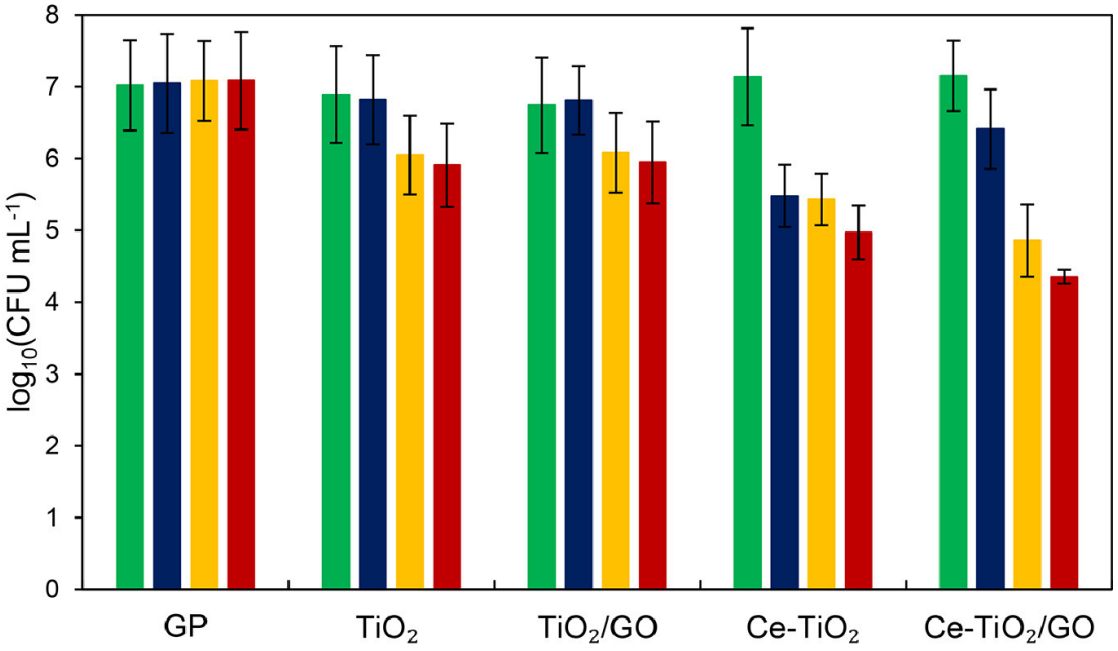

(b) [detached from surface: anode]

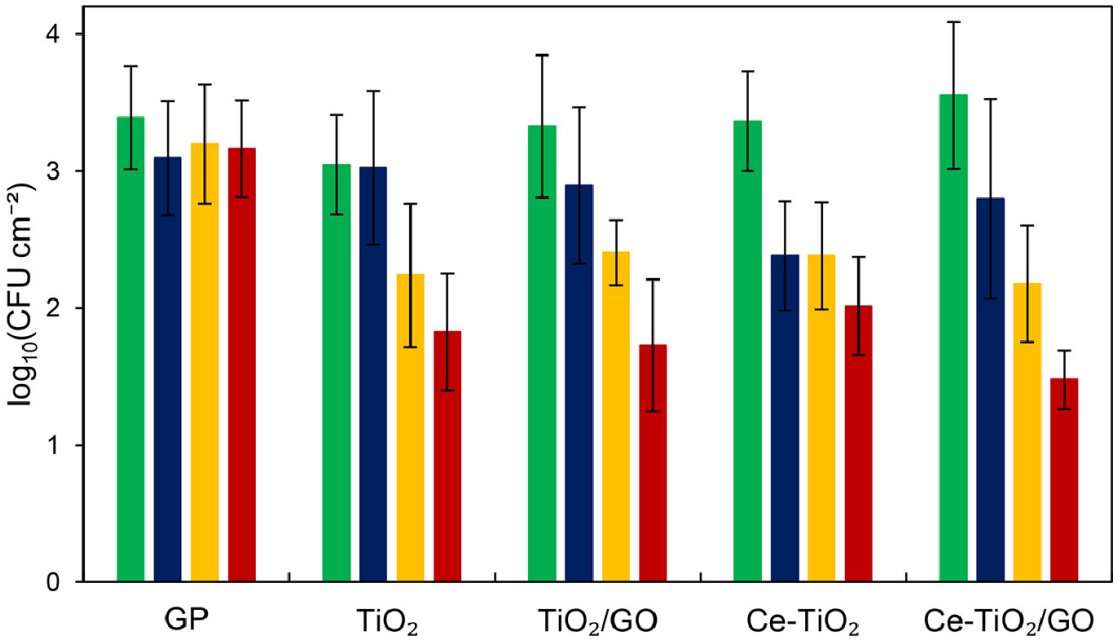

Figure 5: *Colony-forming units (CFU) of S. aureus measured in the liquid medium (a), and detached from the anode surface (b), after no-treatment (Control, green) and electrocatalytic (EC, blue), photocatalytic (PC, yellow) and photoelectrocatalytic (PEC, red) disinfection treatments using GP, TiO_2, TiO_2/GO, Ce-TiO_2 and Ce-TiO_2 anodes. Green, blue, yellow and red squares for control, EC, PC and PEC disinfection treatments, respectively.*

EC treatment, 3-log inactivation efficiency for *E. coli* and MS2 coliphage were obtained in a conventional three-electrode system within 10 min, employing TiO_2 nanotubes on Ti foil photoanode [81]. Similarly, complete inactivation of ARB *E. coli* S1-23 (8-log reduction) was achieved in 10 h by using TNTs in a flow-through thin layer photoreactor for PEC treatment while no obvious effect was observed for PC and EC processes [84]. TiO_2/ITO photoanode fabricated by dip-coating was used for *E. coli* inactivation in simulated wastewater treatment plant effluents (SWTPE), obtaining for PEC an increased bacterial inactivation kinetic constants in comparison to PC from 1.73 up to 2.23×10^4 CFU L^{-1} min^{-1} (3-log reduction in 150 min) [34]. Ag-decorated TiO_2 films on ITO obtained by electrochemical deposition and subsequent impregnation reached a total inactivation of *P. aeruginosa* (6-log) in 5 and 40 min for PEC and PC treatments, respectively [85]. It is worth mentioning that in all these works the applied potential was +1.0 V, considerably higher than that used in the present study (+0.6 V vs. Ag/AgCl). Furthermore, these inactivation studies have been performed in planktonic cells, whereas here exponentially growing cultures of *S. aureus* were allowed colonizing electrode surfaces and forming biofilms for 20 h in the dark. Pires et al. applied Ti/TiO_2-Ag photoanodes to inactivate *Candida parapsilosis stricto sensu* in planktonic and biofilm cells [86]. While inactivation of 10^6 CFU mL^{-1} was achieved in 3 min for planktonic cells, treatments of 60, 10 and 60 min were required for biofilm cells formed on polyvinyl chloride (PVC), silicone, and polytetrafluoroethylene (PTFE), respectively [86]. In the current study, 3-log reduction of *S. aureus* was obtained for pre-colonized Ce-TiO_2/GO anodes after 24 min PEC treatment.

Fig. 6 shows CA curves for the electrosprayed anodes operating at +0.6 V vs. Ag/AgCl as recorded during EC and PEC disinfection treatments. The results of Fig. 6a shows that the incorporation of Ce and GO sheets to TiO_2 increased current density under dark conditions especially for Ce-TiO_2 photocatalyst, meaning enhanced electron transfer through the composite anode. In PEC processes, functionalized anodes exhibited steady photocurrent response, thereby demonstrating good photostability. As displayed in the inset of Fig. 6b, the photocurrent generated increased suddenly at the onset of irradiation. A slightly slower increase was observed for TiO_2/GO photoanodes as compared to pristine TiO_2, becoming even slower with the incorporation of Ce to the composites. This result could be attributed to multi-step charge transportation that retarded charge carrier recombination in TiO_2-based nanocomposites [73,87]. Regarding TiO_2/GO nanocomposite, the multi-step charge transportation consists of photoexcited electrons being transferred from the conduction band of TiO_2 to the GO sheets and, then, to the counter electrode through the external circuit [88]. For Ce-TiO_2 photocatalyst, photoexcited electrons in TiO_2 are promoted to the Ce^{4+}, which is converted to Ce^{3+} transferring the electrons to the counter electrode [49]. In the three-component Ce-TiO_2/GO catalyst, these stages would converge, following the mechanism proposed at the end of this section. Ce-TiO_2/GO presented significantly higher photocurrent response, which could be due to the increase in the number of photogenerated electron-hole pairs and the suppression of their recombination [53, 89, 90].

Bacterial viability was measured by tracking FDA fluorescence for microorganisms after the different disinfection treatments using GP, TiO_2, TiO_2/GO, Ce-TiO_2 and Ce-TiO_2/GO anodes. The results are shown in Fig. 7a and followed the same trend as CFU quantification. After PEC process using all TiO_2-based photocatalytic anodes, a significant decrease of 25–58 % and 21–47 % in the intensity of the FDA signal was obtained compared to EC and PC treatments, respectively ($p < 0.05$). By applying an anodic bias potential, the photogenerated electrons migrate to the external counter electrode, thus facilitating the production of a larger amount of HO· radicals and other ROS due to the inhibition of charge carrier recombination [82, 85]. In addition to HO· generation at the photoanode, carbon-based cathodes (e.g. graphite paper) selectively catalyse O_2 reduction reaction to H_2O_2 and other oxidant species [91, 92]. ROS are able to interact with cell membrane components causing the death of bacteria through oxidative stress [85, 93]. Although ROS are the main radicals responsible for electrodisinfection, reactive chlorine species could be formed from chloride ions in the water, contributing to the inactivation of microorganisms [94, 95]. However, under the experimental conditions employed in this work (+0.6 V vs. Ag/AgCl), reactive chlorine species could not be produced and the main responsible for bacterial impairment is the enhanced production of ROS. DCF fluorescence intensity was measured to check the presence of ROS in the liquid medium during disinfection treatments. The results are shown in Fig. 7b and demonstrated that all treatments led to significant ROS overproduction, which was particularly high for PEC > PC > EC following the same trend observed for CFU and FDA results. The overproduction of intracellular ROS was 28–42 % and 16-27 % higher in PEC in comparison with EC and PC, respectively ($p < 0.05$). Clearly, photogenerated ROS were promoted by the presence of Ce in both Ce-TiO_2 and Ce-TiO_2/GO anodes with respect to bare TiO_2 ($p < 0.05$).

(a) [Electrocatalytic treatment; EC]

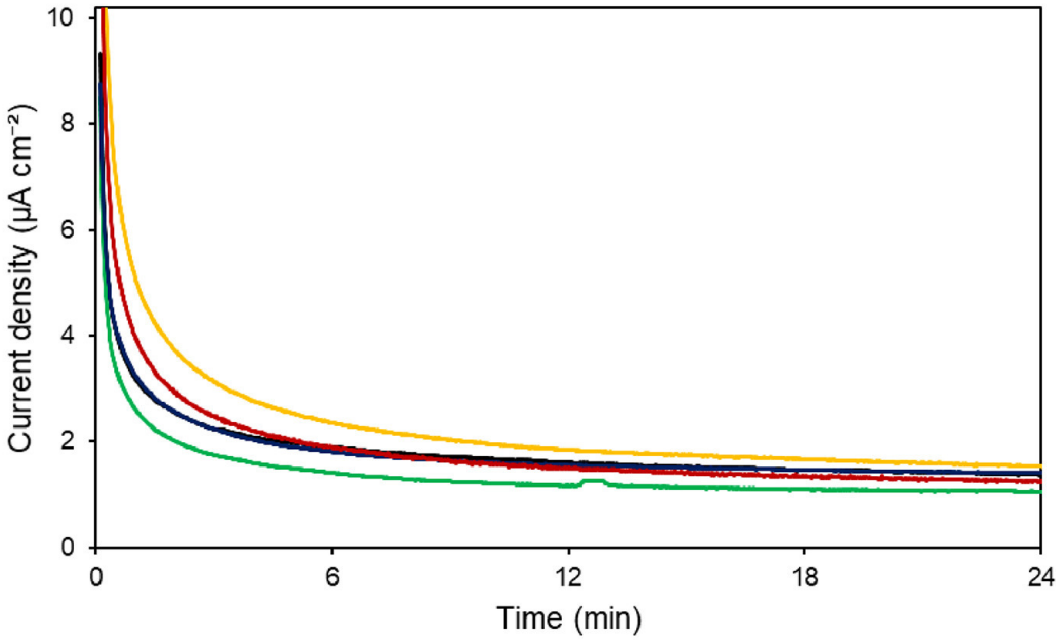

(b) [Photoelectrocatalytic treatment; PEC]

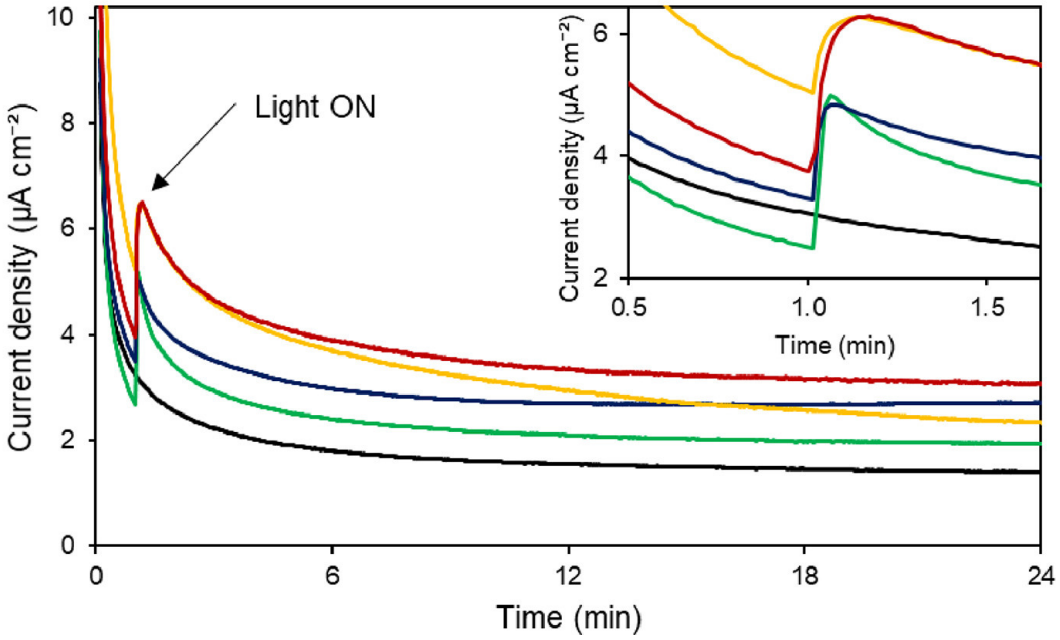

Figure 6: *Chronoamperometry (CA) curves obtained at +0.6 V vs. Ag/AgCl for GP, TiO_2, TiO_2/GO, Ce-TiO_2 and Ce-TiO_2/GO anodes in 1/10 NB during electrocatalytic (a), and photoelectrocatalytic (b) disinfection treatments. Green, blue, yellow and red squares for TiO_2, TiO_2/GO, Ce-TiO_2 and Ce-TiO_2/GO, respectively.*

(a) [FDA]

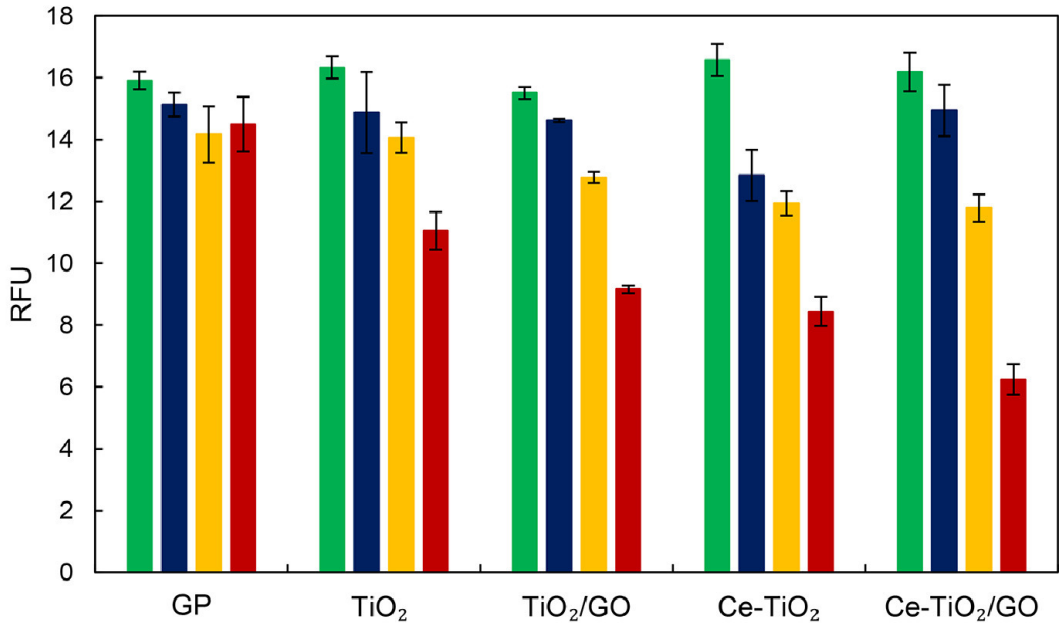

(b) [ROS]

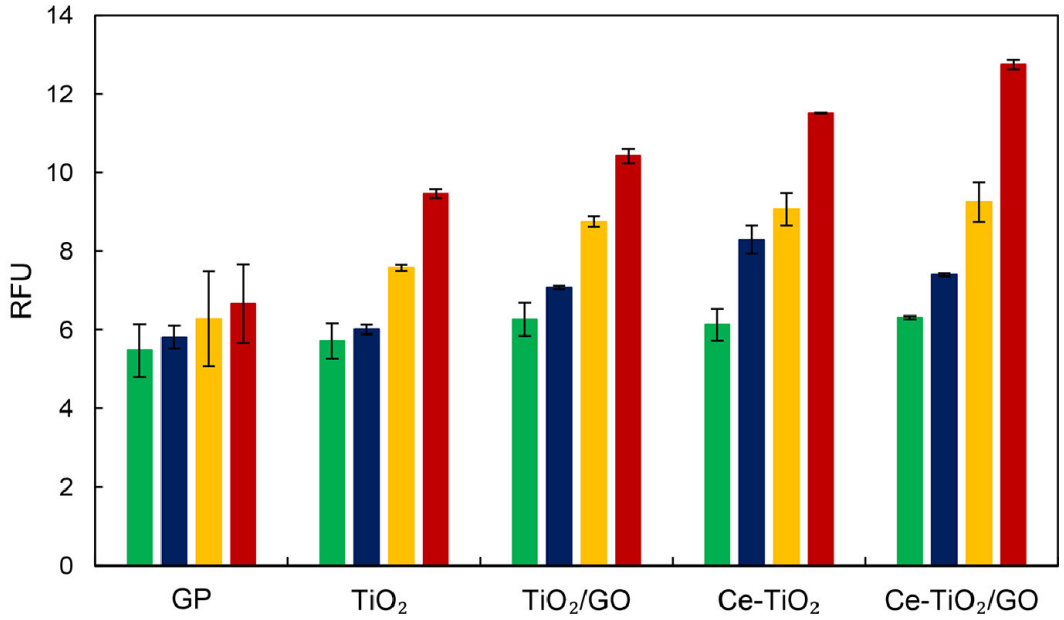

Figure 7: *Relative fluorescence units (RFU) of FDA as cell viability indicator (a), and intracellular DCF due to ROS production (b), in the liquid medium after no-treatment (Control, green), electrocatalytic (EC, blue), photocatalytic (PC, yellow) and photoelectrocatalytic (PEC, red) disinfection treatments using GP,TiO_2, TiO_2/GO, Ce-TiO_2 and Ce-TiO_2/GO anodes. Green, blue, yellow and red squares for control, EC, PC and PEC disinfection treatments, respectively.*

When a semiconductor is irradiated with an energy equivalent to or greater than band-gap, electrons in the valence band (VB) are excited to the conduction band (CB), therefore leaving holes in the VB [96, 97]. Eventually, photogenerated holes can oxidize the water molecule and electrons reduce oxygen, resulting in oxidizing species such as $O_2^{\cdot -}$, $HO^{\cdot}$ and H_2O_2 [85]. Nevertheless, TiO_2 and other semiconductors show fast recombination of electron-hole pairs with a reduced efficiency in ROS production, which can be solved by applying an anodic potential allowing electron extraction through the external circuit [82, 85]. In this work, it has been demonstrated that disinfection performance was significantly enhanced in PEC processes, which can be explained by a more efficient separation of photoinduced charge carriers leading to a higher production of ROS. Ce-TiO_2/GO photoactive anodes exhibited better disinfection performance and higher ROS production than TiO_2, which was attributed to lower electron-hole pairs recombination due to the redox couple Ce^{3+}/Ce^{4+} [90, 98]. The possible mechanism consists in the transfer of photoexcited electrons from TiO_2 to the Ce^{4+} located on the catalytic surface and its subsequent conversion to Ce^{3+}, thus serving as an electron scavenger [49, 50, 99]. Then, the electrons from Ce^{3+} are transferred to the counter electrode through the GO sheets with the help of the outer circuit bias, additionally enhancing charge separation [53, 100, 101]. Moreover, the interchangeable oxidation states of cerium between Ce^{3+} and Ce^{4+} can lead to further production of $O_2^{\cdot -}$ radicals formation by reacting with molecular oxygen [90]. Although it has been reported the effect of electrolyte, photocatalyst and their interactions on the shape of band bending generated to mitigate the space charge [102], Fig. S13 (SM) displays a tentative energy band diagram supporting the proposed mechanism.

4. Conclusions

A sol-gel method was used to synthesize TiO_2 nanoparticles and its composites with Ce (1.5 wt%) and/or GO (2 wt%), obtaining a stable suspension of photoactive particles. The photocatalytic particles were deposited onto graphite paper by electrospray, which allowed creating homogeneous coatings of uniformly distributed aggregates with 1.0–1.5 µm thickness.

LSV and CV showed that photocurrent increased up to about + 0.6 V for TiO_2 and TiO_2/GO anodes and further increased for photocatalysts containing Ce. The highest current density was obtained for Ce-TiO_2/GO composite anodes, attributed to improved charge carrier separation. All functionalized anodes exhibited steady photocurrent response during PEC runs.

Coated anodes were pre-exposed for 20 h to growing cultures of *S. aureus* and further treated for 24 min to evaluate the disinfection capacity of EC, PC and PEC. PEC led to anode surfaces essentially clean from colonizing bacteria outperforming EC and PC. The best results corresponded to Ce-TiO_2/GO anodes with a 3-log reduction in the number of colony-forming cells. A high reduction of the metabolic activity of bacteria in PEC runs, also highest for Ce-TiO_2/GO, confirmed the antimicrobial action of the tested photoanodes.

The impairment of bacterial viability was attributed to the generation of ROS. The highest production of intracellular ROS corresponded to PEC treatments with anodes in the following order: Ce-TiO_2/GO > Ce-TiO_2 > TiO_2/GO > TiO_2. Therefore, the high efficiency of TiO_2-based electrosprayed photoanodes for photoelectrodisinfection in short times (24 min) and under limited irradiance has been demonstrated.

Acknowledgements

This work was supported by the Spanish Ministry of Economy through the project RTI2018-094958-B-I00 MCIU/AEI/FEDER. LV thanks the Spanish Ministry of Education for the FPU Grant FPU17/03096.

References

1. E. Sanganyado, W. Gwenzi. Antibiotic resistance in drinking water systems: occurrence, removal, and human health risks. Sci. Total Environ. 669 (2019), pp. 785-797.
2. J. A. Berkley. Bacterial infections and nutrition: a primer. D.L. Humphries, M.E. Scott, S.H. Vermund (Eds.), Nutrition and Infectious Diseases. Nutrition and Health, Humana-Springer, Cham (2021)
3. S. Mahira, A. Jain, W. Khan, A.J. Domb. Antimicrobial materials-an overview. Antimicrobial Materials for Biomedical Applications, The Royal Society of Chemistry (2019), pp. 1-37.
4. N. A. Lyons, R. Kolter. On the evolution of bacterial multicellularity. Curr. Opin. Microbiol. 24 (2015), pp. 21-28.
5. A. C. Abreu, R. R. Tavares, A. Borges, F. Mergulhão, M. Simões. Current and emergent strategies for disinfection of hospital environments. J. Antimicrob. Chemother. 68 (2013), pp. 2718-2732.
6. W. A. Rutala, D. J. Weber. Disinfection and sterilization: an overview. Am. J. Infect. Control, 41 (2013), pp. S2-S5.

7. M. Wang, M. Ateia, D. Awfa, C. Yoshimura. Regrowth of bacteria after light-based disinfection-what we know and where we go from here. Chemosphere (2020), 128850, 10.1016/j.chemosphere.2020.128850.
8. P. Elena, K. Miri. Formation of contact active antimicrobial surfaces by covalent grafting of quaternary ammonium compounds. Colloids Surf. B, 169 (2018), pp. 195-205.
9. T. J. Silhavy, D. Kahne, S. Walker. The bacterial cell envelope. Cold Spring Harb. Perspect. Biol. 2 (2010), a000414.
10. C. Valotteau, S. Roelants, P. Dasaiyan, S. Zibek, M. Günther, W. Soetaert, B. Everaert, C. M. Pradier, F. Babonneau, N. Baccile, V. Humblot. Antibacterial properties of glycosylated surfaces: variation of the glucosidal moiety and fatty acid conformation of grafted microbial glycolipids. Mol. Syst. Des. Eng. 5 (2020), pp. 1307-1316
11. M. Swaminathan, N.K. Sharma. Antimicrobial activity of the engineered nanoparticles used as coating agents. L. M. T. Martínez, O. V. Kharissova, B. I. Kharisov (Eds.), Handbook of Ecomaterials, Springer International Publishing, Cham (2017), pp. 1-15.
12. B. Ezraty, A. Gennaris, F. Barras, J.F . Collet. Oxidative stress, protein damage and repair in bacteria. Nat. Rev. Microbiol. 15 (2017), pp. 385-396.
13. S. Arango-Santander, A. Pelaez-Vargas, S. C. Freitas, C. García. A novel approach to create an antibacterial surface using titanium dioxide and a combination of dip-pen nanolithography and soft lithography. Sci. Rep. 8 (2018), p. 15818.
14. L. Valenzuela, A. Iglesias-Juez, B. Bachiller-Baeza, M. Faraldos, A. Bahamonde, R. Rosal. Biocide mechanism of highly efficient and stable antimicrobial surfaces based on zinc oxide-reduced graphene oxide photocatalytic coatings. J. Mater. Chem. B, 8 (2020), pp. 8294-8304
15. P. A. Christensen, T. P. Curtis, T. A. Egerton, S. A. M. Kosa, J. R. Tinlin. Photoelectrocatalytic and photocatalytic disinfection of *E. coli* suspensions by titanium dioxide Appl. Catal. B, 41 (2003), pp. 371-386.
16. D. Venieri, E. Chatzisymeon, E. Politi, S. S. Sofianos, A. Katsaounis, D. Mantzavinos. Photoelectrocatalytic disinfection of water and wastewater: performance evaluation by qPCR and culture techniques. J. Water Health, 11 (2013), pp. 21-29.
17. H. Wang, X. Zhang, Y. Su, H. Yu, S. Chen, X. Quan, F. Yang. Photoelectrocatalytic oxidation of aqueous ammonia using TiO_2 nanotube arrays Appl. Surf. Sci. 311 (2014), pp. 851-857.
18. T. A. Egerton, S. A. Kosa, P. A. Christensen. Photoelectrocatalytic disinfection of *E. coli* suspensions by iron doped TiO_2. Phys. Chem. Chem. Phys. 8 (2006), pp. 398-406.
19. M. F. Brugnera, M. Miyata, G. J. Zocolo, L. L. Gonçalves Tessaro, C. Q. Fujimura Leite, M. V. Boldrin Zanoni. A promising technology based on photoelectrocatalysis against Mycobacterium tuberculosis in water disinfection. Environ. Technol. (2019), pp. 1-10.
20. X. Zhang, L. C. Nengzi, B. Li, L. Liu, X. Cheng. Design and construction of a highly efficient photoelectrocatalytic system based on dual-Pd/TNAs photoelectrodes for elimination of triclosan. Sep. Purif. Technol. 235 (2020), 116232.
21. M. Ding, F. Shi, H. Zhu, Y. Yang, J. Zhong, L. Luo, Y. Huo, H. Li. Photoelectrocatalytic bacterial inactivation of Acinetobacter baumannii on Cu_2O/TiO_2@Cu mesh photoanodes. Catal. Sci. Tech. 10 (2020), pp. 7378-7385.
22. R. A. Rather, I. M. C. Lo. Photoelectrochemical sewage treatment by a multifunctional g-C_3N_4/Ag/AgCl/$BiVO_4$ photoanode for the simultaneous degradation of emerging pollutants and hydrogen production, and the disinfection of *E. coli*. Water Res. 168 (2020), 115166.
23. C. Zhang, Y. Jiang, Y. Li, Z. Hu, L. Zhou, M. Zhou. Three-dimensional electrochemical process for wastewater treatment: a general review. Chem. Eng. J. 228 (2013), pp. 455-467.
24. J. Wang, J. A. Jansen, F. Yang. Electrospraying: possibilities and challenges of engineering carriers for biomedical applications-a mini review. Front. Chem. 7 (2019), 258.
25. X. Li, P. Guerieri, W. Zhou, C. Huang, M. R. Zachariah. Direct deposit laminate nanocomposites with enhanced propellent properties. ACS Appl. Mater. Interfaces, 7 (2015), pp. 9103-9109.
26. T. He, J. V. Jokerst. Structured micro/nano materials synthesized via electrospray: a review. Biomater. Sci. 8 (2020), pp. 5555-5573.
27. A. Jaworek. Micro-and nanoparticle production by electrospraying. Powder Technol. 176 (2007), pp. 18-35.
28. T. J. Sill, H. A. von Recum. Electrospinning: applications in drug delivery and tissue engineering. Biomaterials, 29 (2008), pp. 1989-2006.
29. B. Jalvo, M. Faraldos, A. Bahamonde, R. Rosal. Antibacterial surfaces prepared by electrospray coating of photocatalytic nanoparticles. Chem. Eng. J. 334 (2018), pp. 1108-1118.
30. L. Valenzuela, A. Iglesias, M. Faraldos, A. Bahamonde, R. Rosal. Antimicrobial surfaces with self-cleaning properties functionalized by photocatalytic ZnO electrosprayed coatings. J. Hazard.

Mater. 369 (2019), pp. 665-673.

31. X. Liu, Y. Han, G. Li, H. Zhang, H. Zhao. Instant inactivation and rapid decomposition of *Escherichia coli* using a high efficiency TiO_2 nanotube array photoelectrode. RSC Adv. 3 (2013), pp. 20824-20828.
32. C. Pablos, J. Marugán, R. van Grieken, C. Adán, A. Riquelme, J. Palma. Correlation between photoelectrochemical behavior and photoelectrocatalytic activity and scaling-up of P25-TiO_2 electrodes. Electrochim. Acta, 130 (2014), pp. 261-270.
33. M. Zlamal, J. M. Macak, P. Schmuki, J. Krýsa. Electrochemically assisted photocatalysis on self-organized TiO_2 nanotubes. Electrochem. Commun. 9 (2007), pp. 2822-2826.
34. C. Pablos, J. Marugán, C. Adán, M. Osuna, R. van Grieken. Performance of TiO_2 photoanodes toward oxidation of methanol and *E. coli* inactivation in water in a scaled-up photoelectrocatalytic reactor. Electrochim. Acta, 258 (2017), pp. 599-606.
35. Y. Zhu, P. R. Chiarot. Directed assembly of nanomaterials using electrospray deposition and substrate-level patterning. Powder Technol. 364 (2020), pp. 845-850.
36. J. He, Y. Sun, M. Wang, Z. Geng, X. Wu, L. Wang, H. Chen, K. Huang, S. Feng. Direct growth of $NiCo_2O_4$ nanostructure on conductive substrate by electrospray technique for oxygen evolution reaction. J. Alloys Compd. 752 (2018), pp. 389-394.
37. D. H. Kim, M. A. Anderson, W. A. Zeltner. Effects of firing temperature on photocatalytic and photoelectrocatalytic properties of TiO_2. J. Environ. Eng. 121 (1995), pp. 590-594.
38. P. Duan, S. Gao, X. Li, Z. Sun, X. Hu. Preparation of CeO_2-ZrO_2 and titanium dioxide coated carbon nanotube electrode for electrochemical degradation of ceftazidime from aqueous solution. J. Electroanal. Chem. 841 (2019), pp. 10-20.
39. E. Nouri, M. R. Mohammadi, P. Lianos. Impact of preparation method of TiO_2-RGO nanocomposite photoanodes on the performance of dye-sensitized solar cells Electrochim. Acta, 219 (2016), pp. 38-48.
40. E. Castillo-Orozco, A. Kar, R. Kumar. Electrospray mode transition of microdroplets with semiconductor nanoparticle suspension. Sci. Rep. 7 (2017), p. 5144.
41. Y. He, Y. Huang, W. Wang, Y. Cheng. Integrating micromixer precipitation and electrospray drying toward continuous production of drug nanoparticles. Chem. Eng. J. 168 (2011), pp. 931-937.
42. B. Vonnegut, R. L. Neubauer. Production of monodisperse liquid particles by electrical atomization. J. Colloid Sci. 7 (1952), pp. 616-622.
43. A. Gomes, E. Fernandes, J. L. F. C. Lima. Fluorescence probes used for detection of reactive oxygen species. J. Biochem. Biophys. Methods, 65 (2005), pp. 45-80.
44. B. Kalyanaraman, V. Darley-Usmar, K. J. A. Davies, P. A. Dennery, H. J. Forman, M. B. Grisham, G. E. Mann, K. Moore, L. J. Roberts, H. Ischiropoulos. Measuring reactive oxygen and nitrogen species with fluorescent probes: challenges and limitations. Free Radic. Biol. Med. 52 (2012), pp. 1-6.
45. A. Jaworek, A. T. Sobczyk. Electrospraying route to nanotechnology: an overview. J. Electrostat. 66 (2008), pp. 197-219.
46. Á. G. Marín, I. G. Loscertales, A. Barrero. Surface tension effects on submerged electrosprays. Biomicrofluidics, 6 (2012), 044104.
47. J. A. Tapia-Hernández, P. I. Torres-Chávez, B. Ramírez-Wong, A. Rascón-Chu, M. Plascencia-Jatomea, C. G. Barreras-Urbina, N. A. Rangel-Vázquez, F. Rodríguez-Félix. Micro-and nanoparticles by electrospray: advances and applications in foods. J. Agric. Food Chem. 63 (2015), pp. 4699-4707.
48. T. X. Liu, X. Z. Li, F. B. Li. Enhanced photocatalytic activity of Ce^{3+}-TiO_2 hydrosols in aqueous and gaseous phases. Chem. Eng. J. 157 (2010), pp. 475-482.
49. X. Fan, J. Wan, E. Liu, L. Sun, Y. Hu, H. Li, X. Hu, J. Fan. High-efficiency photoelectrocatalytic hydrogen generation enabled by Ag deposited and Ce doped TiO_2. Ceram. Int. 41 (2015), pp. 5107-5116.
50. T. Tong, J. Zhang, B. Tian, F. Chen, D. He, M. Anpo. Preparation of Ce–TiO_2 catalysts by controlled hydrolysis of titanium alkoxide based on esterification reaction and study on its photocatalytic activity. J. Colloid Interface Sci. 315 (2007), pp. 382-388.
51. A. Escobedo-Morales, I. I. Ruiz-López, M. D. Ruiz-Peralta, L. Tepech-Carrillo, M. Sánchez-Cantú, J. E. Moreno-Orea. Automated method for the determination of the band gap energy of pure and mixed powder samples using diffuse reflectance spectroscopy. Heliyon, 5 (2019), p. e01505.
52. P. Makuła, M. Pacia, W. Macyk. How to correctly determine the band gap energy of modified semiconductor photocatalysts based on UV-vis spectra. J. Phys. Chem. Lett. 9 (2018), pp. 6814-6817.

53. P. Seeharaj, P. Kongmun, P. Paiplod, S. Prakobmit, C. Sriwong, P. Kim-Lohsoontorn, N. Vittayakorn. Ultrasonically-assisted surface modified TiO_2/rGO/CeO_2 heterojunction photocatalysts for conversion of CO_2 to methanol and ethanol. Ultrason. Sonochem. 58 (2019), 104657.
54. J. Shen, B. Yan, M. Shi, H. Ma, N. Li, M. Ye. One step hydrothermal synthesis of TiO_2-reduced graphene oxide sheets J. Mater. Chem. 21 (2011), pp. 3415-3421.
55. Y. Wang, M. Zhang, H. Yu, Y. Zuo, J. Gao, G. He, Z. Sun. Facile fabrication of Ag/graphene oxide/TiO_2 nanorod array as a powerful substrate for photocatalytic degradation and surface-enhanced Raman scattering detection. Appl. Catal. B, 252 (2019), pp. 174-186.
56. J. C. Cano-Franco, M. Álvarez-Láinez. Effect of CeO_2 content in morphology and optoelectronic properties of TiO_2-CeO_2 nanoparticles in visible light organic degradation. Mat. Sci. Semicond. Proc. 90 (2019), pp. 190-197.
57. G. Mogilevsky, O. Hartman, E. D. Emmons, A. Balboa, J. B. DeCoste, B. J. Schindler, I. Iordanov, C. J. Karwacki. Bottom-up synthesis of anatase nanoparticles with graphene domains. ACS Appl. Mater. Interfaces, 6 (2014), pp. 10638-10648.
58. B. Elgh, A. E .C. Palmqvist. Controlling anatase and rutile polymorph selectivity during low-temperature synthesis of mesoporous TiO_2 films. J. Mater. Chem. A, 2 (2014), pp. 3024-3030.
59. T. S. Sakthivel, S. Das, C. J. Pratt, S. Seal. One-pot synthesis of a ceria–graphene oxide composite for the efficient removal of arsenic species. Nanoscale, 9 (2017), pp. 3367-3374.
60. J. Zhang, P. Zhou, J. Liu, J. Yu. New understanding of the difference of photocatalytic activity among anatase, rutile and brookite TiO_2. Phys. Chem. Chem. Phys. 16 (2014), pp. 20382-20386.
61. J. Yu, J. Fan, B. Cheng. Dye-sensitized solar cells based on anatase TiO_2 hollow spheres/carbon nanotube composite films. J. Power Sources, 196 (2011), pp. 7891-7898.
62. J. Yu, T. Ma, S. Liu. Enhanced photocatalytic activity of mesoporous TiO_2 aggregates by embedding carbon nanotubes as electron-transfer channel. Phys. Chem. Chem. Phys. 13 (2011), pp. 3491-3501.
63. J. Yan, G. Wu, N. Guan, L. Li, Z. Li, X. Cao. Understanding the effect of surface/bulk defects on the photocatalytic activity of TiO_2: anatase versus rutile. Phys. Chem. Chem. Phys. 15 (2013), pp. 10978-10988.
64. A. Kaniyoor, T. T. Baby, S. Ramaprabhu. Graphene synthesis via hydrogen induced low temperature exfoliation of graphite oxide. J. Mater. Chem. 20 (2010), pp. 8467-8469.
65. Y. Cheng, M. Zhang, G. Yao, L. Yang, J. Tao, Z. Gong, G. He, Z. Sun. Band gap manipulation of cerium doping TiO_2 nanopowders by hydrothermal method. J. Alloys Compd. 662 (2016), pp. 179-184.
66. S. M. Lee, H. H. Lee, S. C. Hong. Influence of calcination temperature on Ce/TiO_2 catalysis of selective catalytic oxidation of NH_3 to N_2. Appl. Catal. A, 470 (2014), pp. 189-198.
67. H. Yang, K. Zhang, R. Shi, A. Tang. Sol-gel synthesis and photocatalytic activity of CeO_2/TiO_2 nanocomposites J. Am. Ceram. Soc. 90 (2007), pp. 1370-1374
68. A. Hosseini, K.Ç. Içli, M. Özenbaş, Ç. Erçelebi. Fabrication and characterization of spin-coated TiO_2 films. Energy Procedia, 60 (2014), pp. 191-198.
69. A. Makishima, H. Sakamoto, J. Qiu. The preparation and surface roughness of CeO_2–TiO_2 films by a sol-gel spin-coating process. J. Non Cryst. Solids, 349 (2004), pp. 355-359.
70. A. P. Borole, G. Reguera, B. Ringeisen, Z. W. Wang, Y. Feng, B. H. Kim. Electroactive biofilms: current status and future research needs. Energy Environ. Sci. 4 (2011), pp. 4813-4834.
71. N. S. Malvankar, M. T. Tuominen, D. R. Lovley. Biofilm conductivity is a decisive variable for high-current-density *Geobacter sulfurreducens* microbial fuel cells. Energy Environ. Sci. 5 (2012), pp. 5790-5797.
72. G. Chen. Electrochemical technologies in wastewater treatment. Sep. Purif. Technol. 38 (2004), pp. 11-41.
73. S. Halevy, E. Korin, A. Bettelheim. Enhancement of photoelectrochemical organics degradation and power generation by electrodeposited coatings of g-C_3N_4 and graphene on TiO_2 nanotube arrays. Nanoscale Adv. 1 (2019), pp. 4128-4136.
74. C. Jeganathan, T. C. Sabari Girisun, S. Vijaya, S. Anandan. Improved charge collection and photo conversion of bacteriorhodopsin sensitized solar cells coupled with reduced graphene oxide decorated one-dimensional TiO_2 nanorod hybrid photoanodes. Electrochim. Acta, 319 (2019), pp. 909-921.
75. X. Cao, X. Yang, H. Li, W. Huang, X. Liu. Investigation of Ce-TiO_2 photocatalyst and its application in asphalt-based specimens for NO degradation. Constr. Build. Mater. 148 (2017), pp. 824-832.
76. D. Dworschak, C. Brunnhofer, M. Valtiner. Photocorrosion of ZnO single crystals during electrochemical water splitting. ACS Appl. Mater.

Interfaces, 12 (2020), pp. 51530-51536.

77. H. Fu, T. Xu, S. Zhu, Y. Zhu. Photocorrosion inhibition and enhancement of photocatalytic activity for ZnO via hybridization with C60. Environ. Sci. Technol. 42 (2008), pp. 8064-8069.
78. M. A. Ehsan, R. Naeem, A. Rehman, A. S. Hakeem, M. Mazhar. Facile fabrication of CeO_2-TiO_2 thin films via solution based CVD and their photoelectrochemical studies. J. Mater. Sci. Mater. Electron. 29 (2018), pp. 13209-13219.
79. Y. Tang, L. Liu, H. Zhao, D. Jia, X. Xie, Y. Zhang, X. Li. Anatase/rutile titania anchored carbon nanotube porous nanocomposites as superior anodes for lithium ion batteries. CrystEngComm, 18 (2016), pp. 4489-4494.
80. M. Salari, S. H. Aboutalebi, A. T. Chidembo, I. P. Nevirkovets, K. Konstantinov, H. K. Liu. Enhancement of the electrochemical capacitance of TiO_2 nanotube arrays through controlled phase transformation of anatase to rutile. Phys. Chem. Chem. Phys. 14 (2012), pp. 4770-4779.
81. K. Cho, S. Lee, H. Kim, H.E. Kim, A. Son, E.J. Kim, M. Li, Z. Qiang, S. W. Hong. Effects of reactive oxidants generation and capacitance on photoelectrochemical water disinfection with self-doped titanium dioxide nanotube arrays. Appl. Catal. B, 257 (2019), 117910.
82. S. McMichael, M. Waso, B. Reyneke, W. Khan, J. A. Byrne, P. Fernández-Ibáñez. Electrochemically assisted photocatalysis for the disinfection of rainwater under solar irradiation. Appl. Catal. B, 281 (2021), 119485.
83. I. Salmerón, P. K. Sharma, M. I. Polo-López, A. Tolosana, S. McMichael, I. Oller, J. A. Byrne, P. Fernández-Ibáñez. Electrochemically assisted photocatalysis for the simultaneous degradation of organic micro-contaminants and inactivation of microorganisms in water. Process Saf. Environ. Prot. 147 (2021), pp. 488-496.
84. Q. Jiang, H. Yin, G. Li, H. Liu, T. An, P. K. Wong, H. Zhao. Elimination of antibiotic-resistance bacterium and its associated/dissociative bla_{TEM-1} and *aac(3)-II* antibiotic-resistance genes in aqueous system via photoelectrocatalytic process. Water Res. 125 (2017), pp. 219-226.
85. R. B. Domínguez-Espíndola, C. Bruguera-Casamada, S. Silva-Martínez, R. M. Araujo, E. Brillas, I. Sirés. Photoelectrocatalytic inactivation of *Pseudomonas aeruginosa* using an Ag-decorated TiO_2 photoanode. Sep. Purif. Technol. 208 (2019), pp. 83-91.
86. R. H. Pires, M. F. Brugnera, M. V. B. Zanoni, M. J. S. M. Giannini. Effectiveness of photoelectrocatalysis treatment for the inactivation of *Candida parapsilosis* sensu stricto in planktonic cultures and biofilms. Appl. Catal. A, 511 (2016), pp. 149-155.
87. H. Dotan, K. Sivula, M. Grätzel, A. Rothschild, S.C. Warren. Probing the photoelectrochemical properties of hematite (α-Fe_2O_3) electrodes using hydrogen peroxide as a hole scavenger. Energy Environ. Sci. 4 (2011), pp. 958-964.
88. J. S. Yang, W. W. P. Lai, S. C. Panchangam, A. Y. C. Lin. Photoelectrochemical degradation of perfluorooctanoic acid (PFOA) with GOP25/FTO anodes: Intermediates and reaction pathways. J. Hazard. Mater. 391 (2020), 122247.
89. N. Ahmadi, M. Bagherzadeh, A. Nemati. Comparison between electrochemical and photoelectrochemical detection of dopamine based on titania-ceria-graphene quantum dots nanocomposite. Biosens. Bioelectron. 151 (2020), 111977.
90. Q. Zhou, A. Xing, J. Li, D. Zhao, K. Zhao, M. Lei. Synergistic enhancement in photoelectrocatalytic degradation of bisphenol A by CeO_2 and reduced graphene oxide co-modified TiO_2 nanotube arrays in combination with Fenton oxidation. Electrochim. Acta, 209 (2016), pp. 379-388.
91. P. Ma, H. Ma, A. Galia, S. Sabatino, O. Scialdone. Reduction of oxygen to $H_2O_2$2 at carbon felt cathode in undivided cells. Effect of the ratio between the anode and the cathode surfaces and of other operative parameters. Sep. Purif. Technol. 208 (2019), pp. 116-122.
92. Y. Sun, I. Sinev, W. Ju, A. Bergmann, S. Dresp, S. Kühl, C. Spöri, H. Schmies, H. Wang, D. Bernsmeier, B. Paul, R. Schmack, R. Kraehnert, B. Roldan Cuenya, P. Strasser. Efficient electrochemical hydrogen peroxide production from molecular oxygen on nitrogen-doped mesoporous carbon catalysts. ACS Catal. 8 (2018), pp. 2844-2856.
93. H. A. Foster, I. B. Ditta, S. Varghese, A. Steele. Photocatalytic disinfection using titanium dioxide: spectrum and mechanism of antimicrobial activity. Appl. Microbiol. Biotechnol. 90 (2011), pp. 1847-1868.
94. M. S. Koo, X. Chen, K. Cho, T. An, W. Choi. In situ photoelectrochemical chloride activation using a WO_3 electrode for oxidative treatment with simultaneous H_2 evolution under visible light. Environ. Sci. Technol. 53 (2019), pp. 9926-9936.
95. D. Rajkumar, J. G. Kim. Oxidation of various reactive dyes with *in situ* electro-generated active chlorine for textile dyeing industry wastewater treatment. J. Hazard. Mater. 136 (2006), pp. 203-212.

96. S. Garcia-Segura, E. Brillas. Applied photoelectrocatalysis on the degradation of organic pollutants in wastewaters. J. Photochem. Photobiol. C, 31 (2017), pp. 1-35.
97. M. Pelaez, N. T. Nolan, S. C. Pillai, M. K. Seery, P. Falaras, A. G. Kontos, P. S. M. Dunlop, J. W. J. Hamilton, J.A. Byrne, K. O'Shea, M. H. Entezari, D. D. Dionysiou. A review on the visible light active titanium dioxide photocatalysts for environmental applications. Appl. Catal. B, 125 (2012), pp. 331-349.
98. R. Hassandoost, S. R. Pouran, A. Khataee, Y. Orooji, S. W. Joo. Hierarchically structured ternary heterojunctions based on Ce^{3+}/Ce^{4+} modified Fe_3O_4 nanoparticles anchored onto graphene oxide sheets as magnetic visible-light-active photocatalysts for decontamination of oxytetracycline. J. Hazard. Mater. 376 (2019), pp. 200-211.
99. Q. Z. Yan, X. T. Su, Z. Y. Huang, C. C. Ge. Sol-gel auto-igniting synthesis and structural property of cerium-doped titanium dioxide nanosized powders. J. Eur. Ceram. Soc. 26 (2006), pp. 915-921.
100. M. Tayebi, M. Kolaei, A. Tayyebi, Z. Masoumi, Z. Belbasi, B. K. Lee. Reduced graphene oxide (RGO) on TiO_2 for an improved photoelectrochemical (PEC) and photocatalytic activity. Sol. Energy, 190 (2019), pp. 185-194.
101. Y. Wang, X. Wang, M. Zhang, L. Fang, L. Jin, J. Gao, Y. Zhang, B. Yang, G. He, Z. Sun. TiO_2 nanorod array film decorated with rGO nanosheets for enhancing photocatalytic and photoelectrochemical properties. J. Alloys Compd. 770 (2019), pp. 243-251.
102. Z. Zhang, J. T. Yates. Band bending in semiconductors: chemical and physical consequences at surfaces and interfaces. Chem. Rev. 112 (2012), pp. 5520-5551.

Supplementary Materials

High performance of electrosprayed graphene oxide/TiO_2/Ce-TiO_2 photoanodes for photoelectrocatalytic inactivation of *S. aureus*

Laura Valenzuela[1,*], Marisol Faraldos[2], Ana Bahamonde[2], and Roberto Rosal[1]

[1]Department of Chemical Engineering, University of Alcalá, Alcalá de Henares, Madrid E-28871, Spain
[2]Instituto de Catálisis y Petroleoquímica, ICP-CSIC, Marie Curie 2, Madrid E-28049, Spain

Contents:

* Corresponding author: laura.valenzuela@uah.es

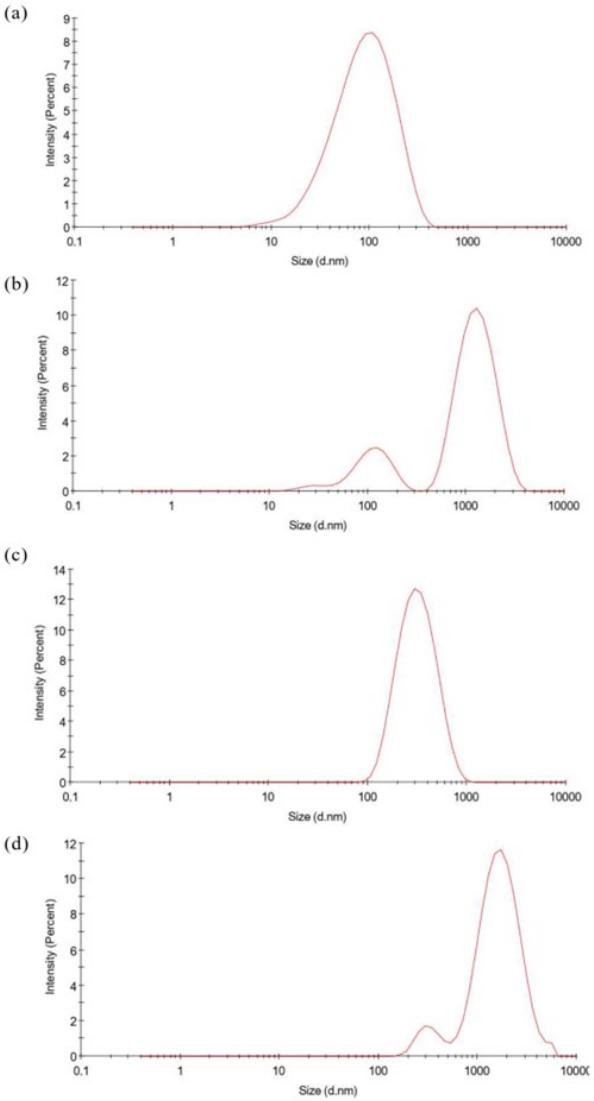

Figure S1: *DLS particle size measurements of TiO_2 (a), TiO_2/GO (b), Ce-TiO_2 (c), and Ce-TiO_2/GO (d) photocatalytic suspensions.*

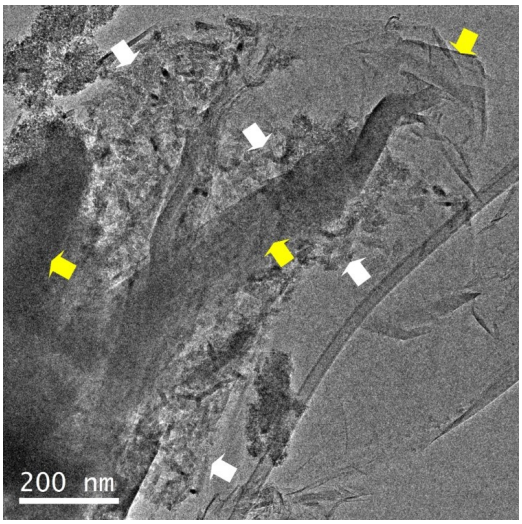

Figure S2: *TEM image showing Ce-TiO_2 particles (white arrows) and GO sheets (yellow arrows) in a Ce-TiO_2/GO photocatalyst.*

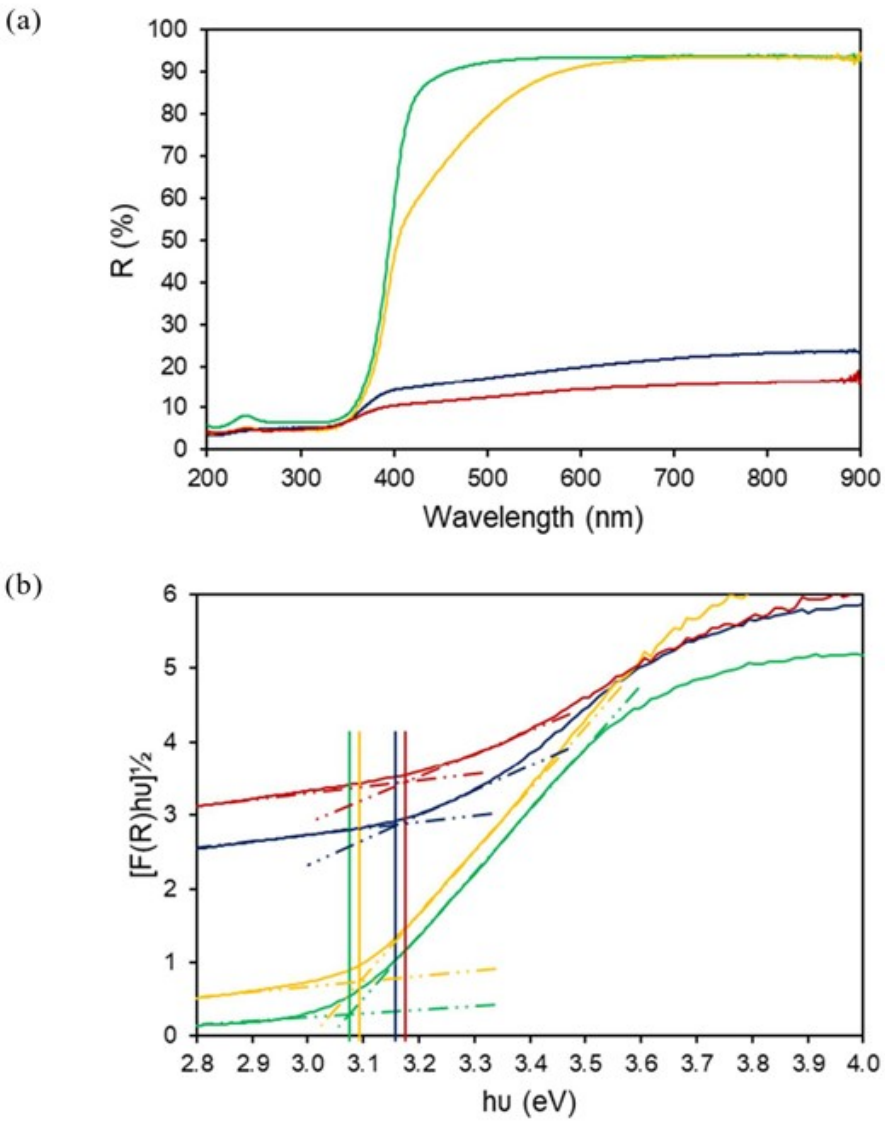

Figure S3: *UV-vis diffuse reflectance (a) and Tauc plots combined with baseline method of Kubelka-Munk function (b) for TiO_2 (green), TiO_2/GO (blue), Ce-TiO_2 (yellow) and Ce-TiO_2/GO (red).*

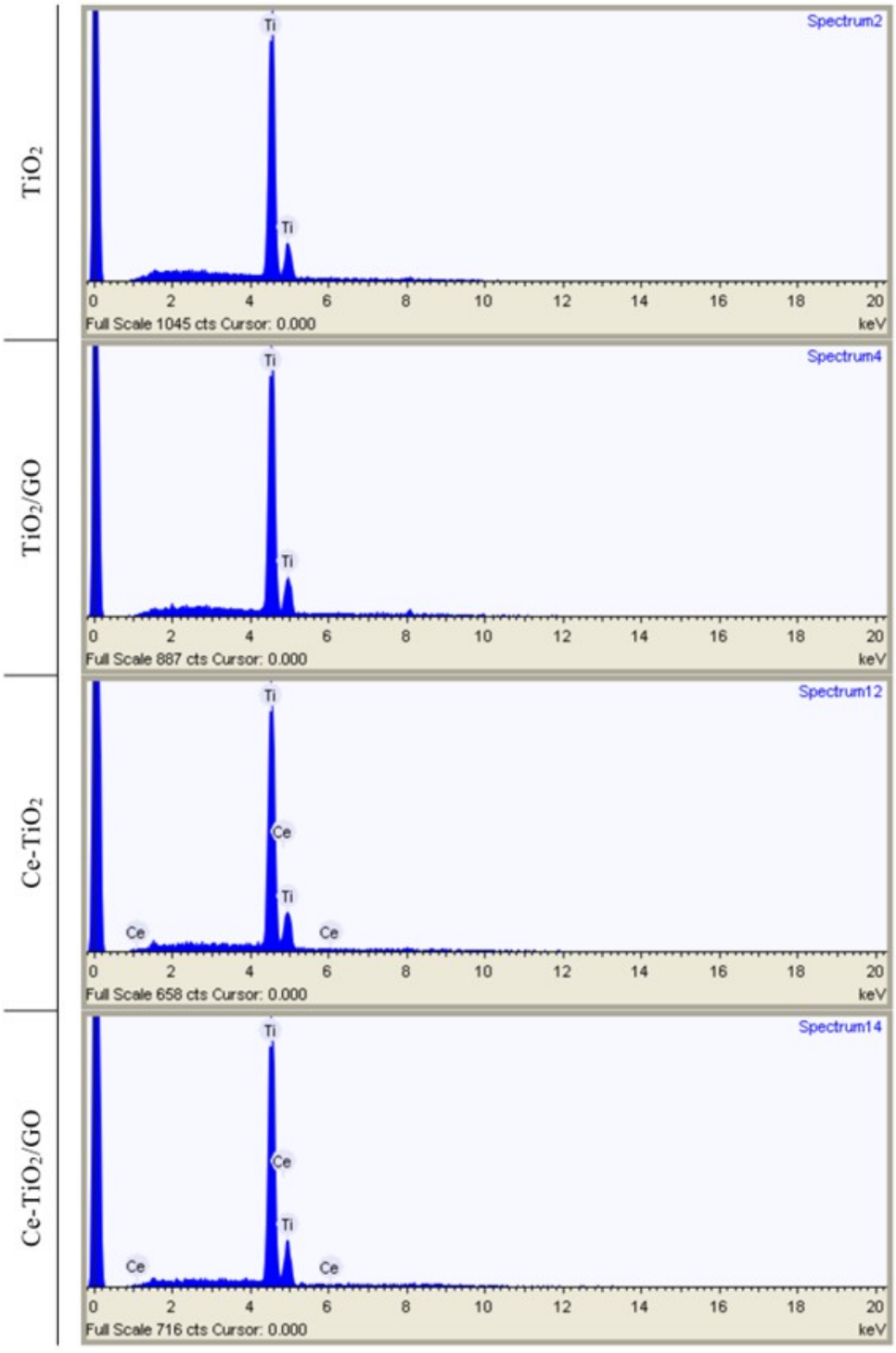

Figure S4: *EDX spectra of TiO_2, TiO_2/GO, Ce-TiO_2 and Ce-TiO_2/GO photocatalytic materials.*

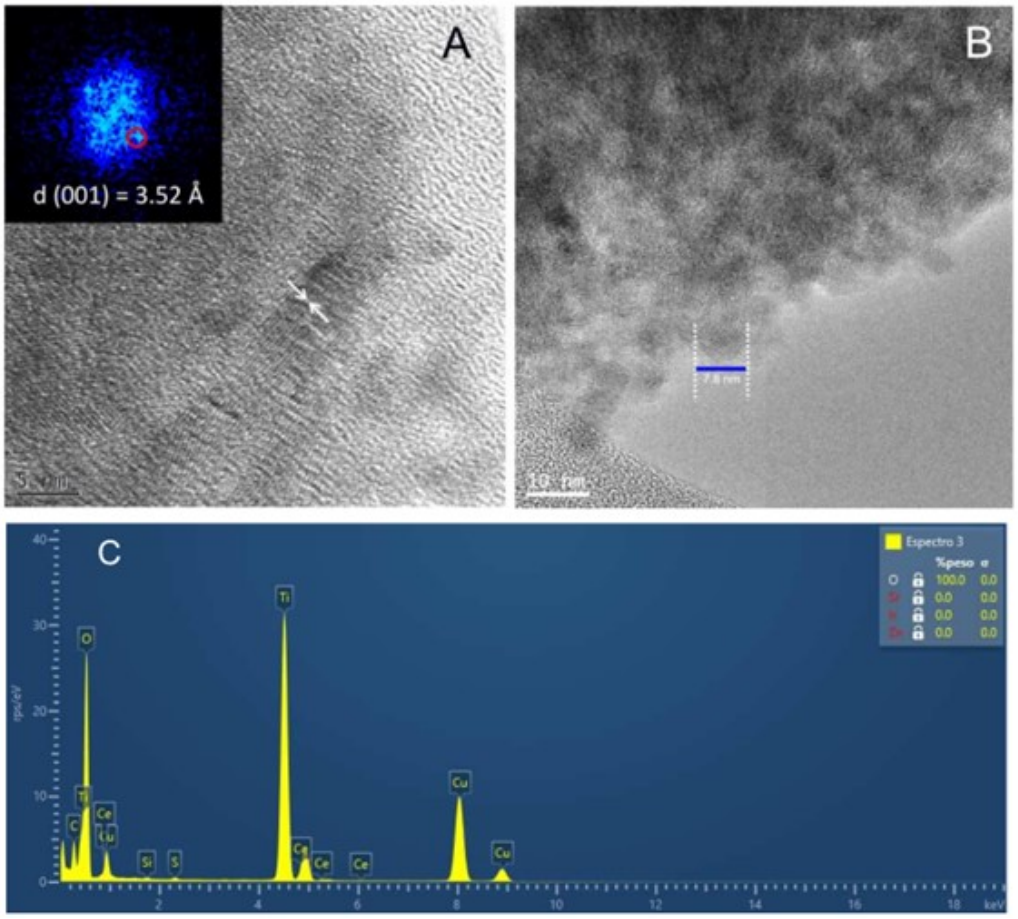

Figure S5: *TEM images showing lattice spacing of anatase crystalline phase (A), crystallite size (B), and the EDX spectrum of Ce-TiO_2 photocatalyst (C). (Cu is from grid).*

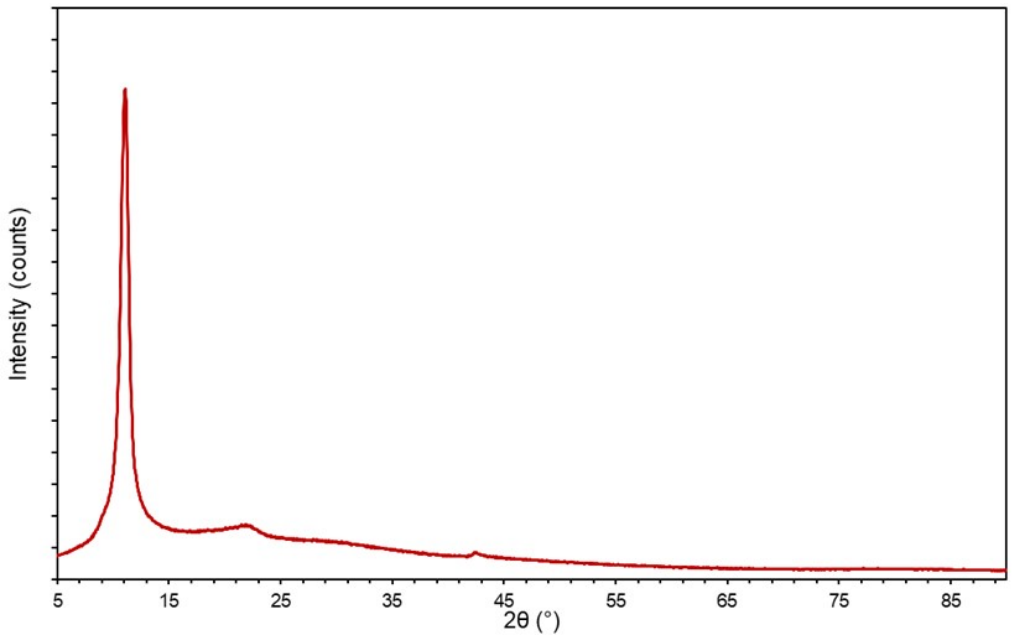

Figure S6: *X-ray diffraction pattern of GO (Graphenea, Spain).*

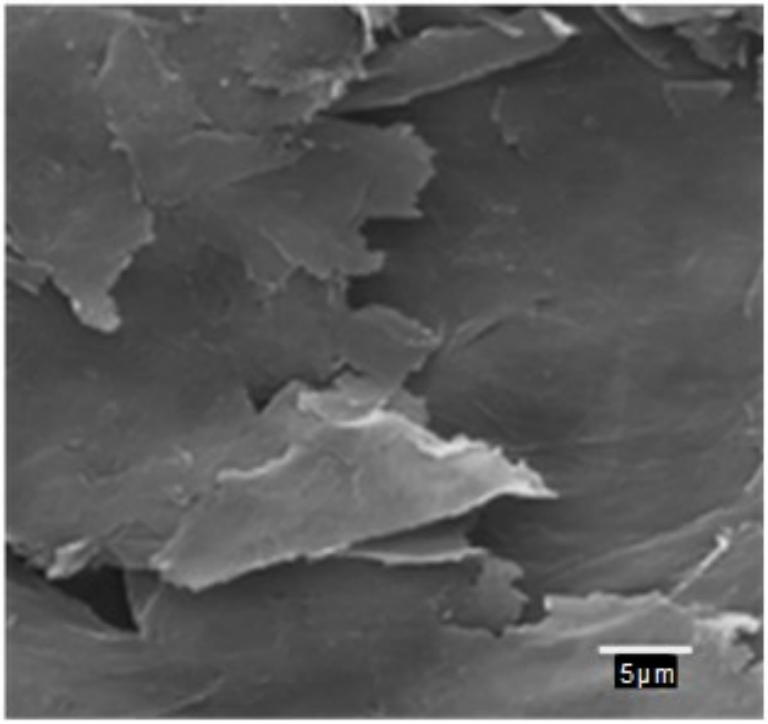

Figure S7: *SEM image of sanded graphite paper (GP).*

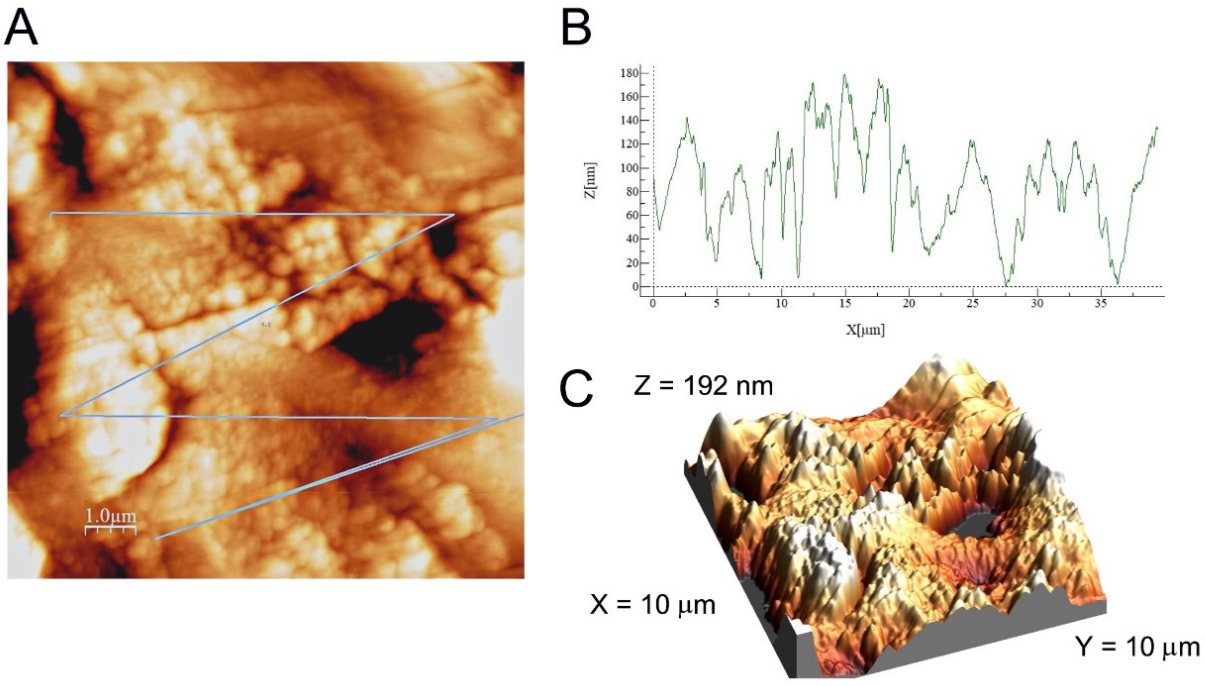

Figure S8: *AFM image (A), profile along the trajectory shown in the figure (B), and 3D view of a specimen from Ce-TiO_2/GO photocatalytic anode (C).*

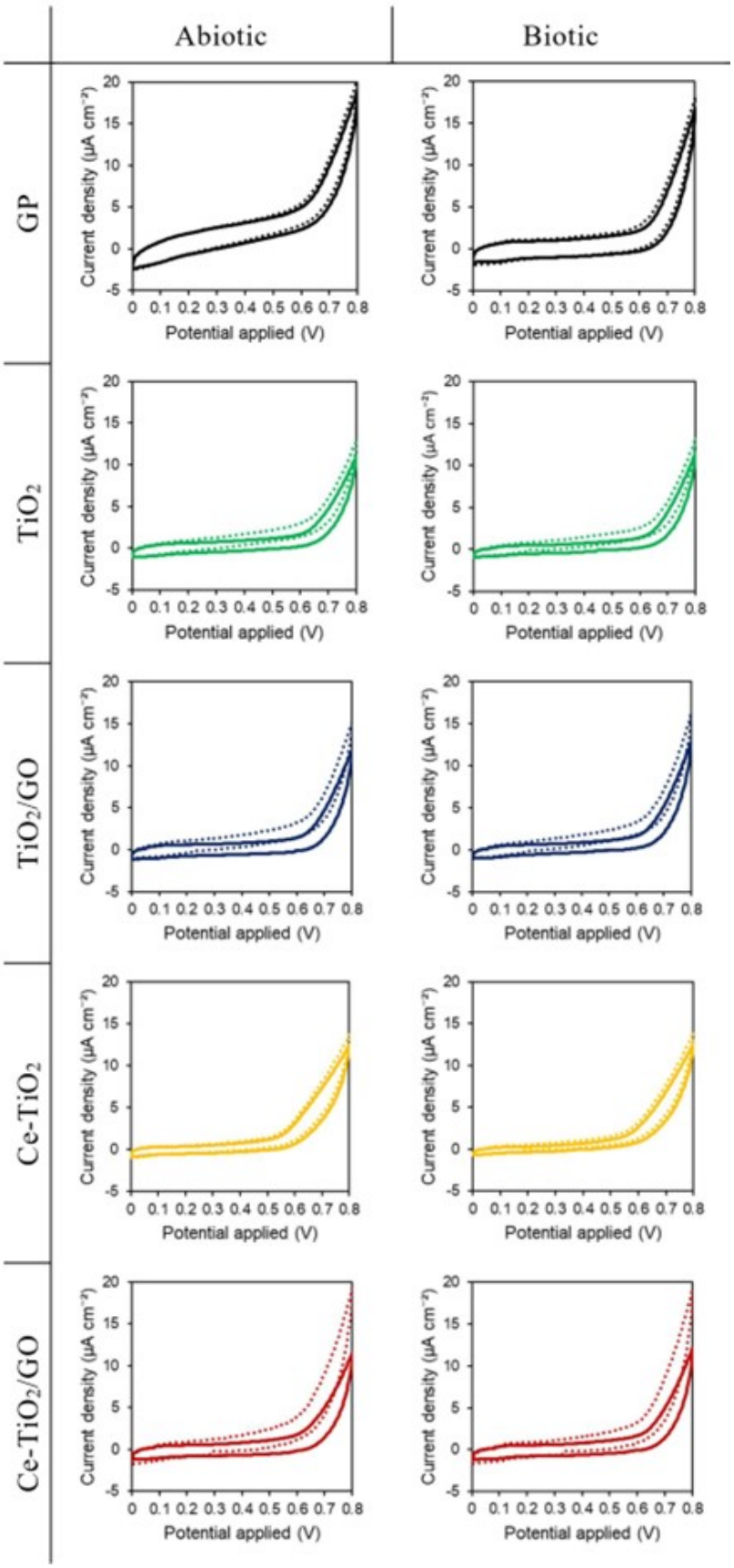

Figure S9: *Cyclic voltammetry (CV) curves of GP (black), TiO_2 (green), TiO_2/GO (blue), Ce-TiO_2 (yellow) and Ce-TiO_2/GO (red) anodes in 1/10 NB at 5 mV s^{-1} under abiotic and biotic conditions in the absence (-) and presence (...) of UV light irradiation. The fifth CV scan is displayed.*

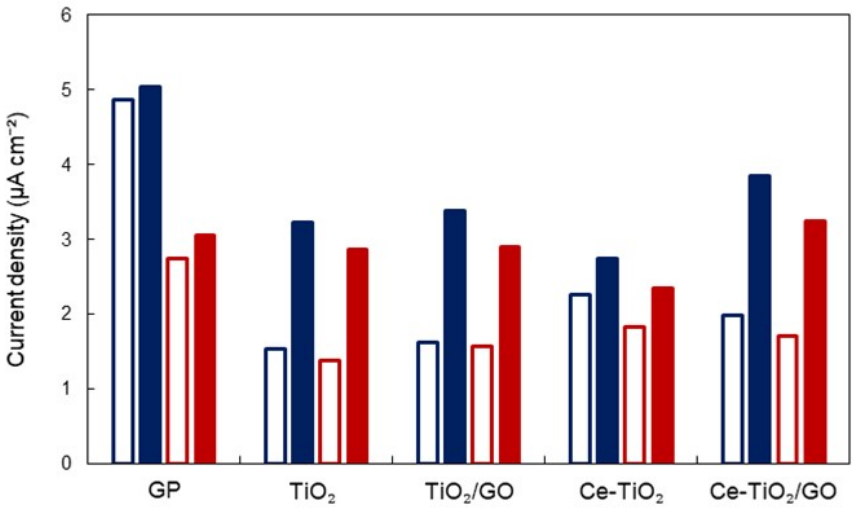

Figure S10: *Current density values at +0.6 V vs. Ag/AgCl obtained from linear sweep voltammetry (LSV) curves of GP, $TiO_2$2, TiO_2/GO, Ce-TiO_2 and Ce-TiO_2/GO anodes in 1/10 NB at 5 mV s^{-1} under abiotic (blue) and biotic (red) conditions in the absence (empty) and presence (filled) of UV light irradiation.*

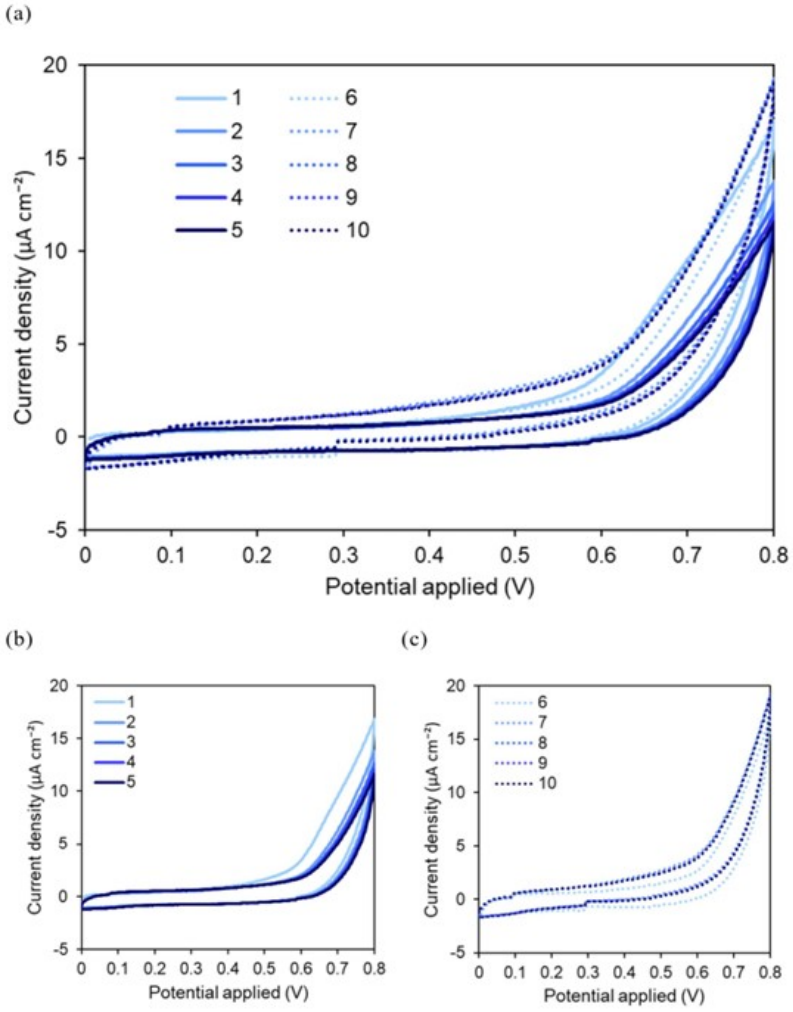

Figure S11: *Overlay Cyclic Voltammetry (CV) curves for the ten cycles performed with Ce-TiO_2/GO anode under abiotic conditions in the absence (-) and presence (...) of UV light irradiation (a), overlay CV curves for 1st-5th cycle conducted in the dark (b), and overlay CV curves for 6th-10th cycle carried out under UV light irradiation.*

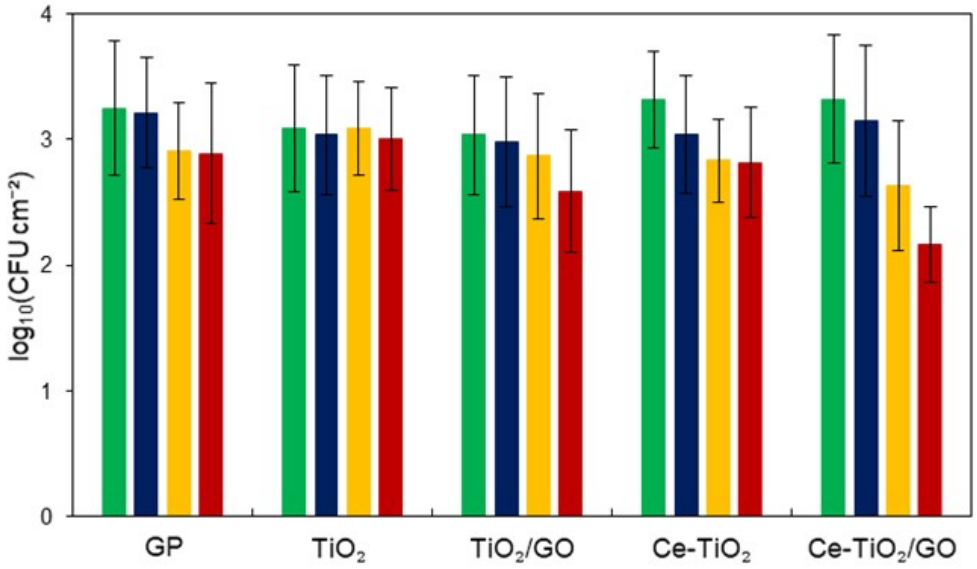

Figure S12: *Colony-forming units (CFU) of S. aureus measured from the cathode surface after no-treatment (Control, green) and electrocatalytic (EC, blue), photocatalytic (PC, yellow) and photoelectrocatalytic (PEC, red) disinfection treatments using GP, TiO_2, TiO_2/GO, Ce-TiO_2 and Ce-TiO_2/GO anodes.*

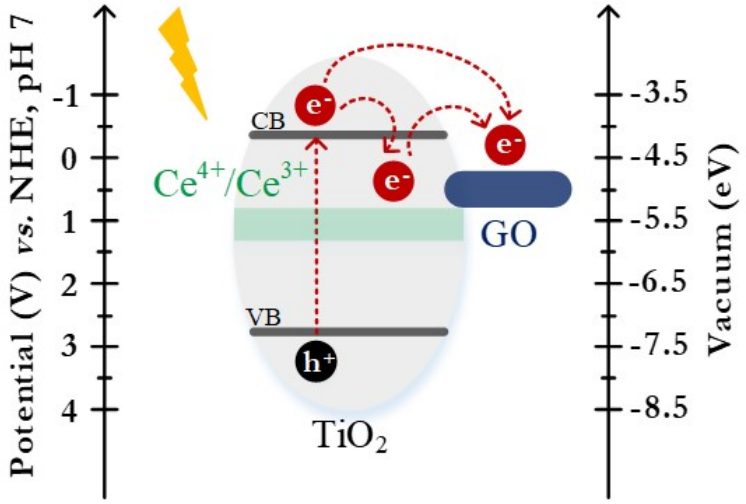

Figure S13: *Proposed energy band diagram representing the electron transfer mechanism in the Ce-TiO_2/GO photocatalyst.*